Autism-like phenotypes and increased NMDAR2D expression in mice with KDM5B histone lysine demethylase deficiency

Leticia Pérez-Sisqués[1,2], Shail U. Bhatt[1], Angela Caruso[3], Josephine L. Robb[4], Alex P.A. Donovan[5], Rosemary Bamford[4], Alejo Torres-Cano[6], Shoshana Spring[7], Eleanor Hendy[4], Talia E. Gileadi[1], Martyna Panasiuk[2], Jed Trengove[4], Neeru Jindal[4], Mohi U. Ahmed[1], Joyce Taylor-Papadimitriou[8], Diana Cash[9], Nicholas Clifton[4], Jacob Ellegood[7,10], Laura C. Andreae[2], Jason P. Lerch[7,11], Maria Luisa Scattoni[3], K. Peter Giese[12], Cathy Fernandes[13] and M. Albert Basson[1,2,4*]

[1] Centre for Craniofacial and Regenerative Biology, Guy's Hospital, King's College London, London SE1 9RT, UK
[2] MRC Centre for Neurodevelopmental Disorders, New Hunt's House, King's College London, London SE1 1UL, UK
[3] Research Coordination and Support Service, Istituto Superiore di Sanità, 00161 Rome, Italy
[4] Clinical and Biomedical Sciences, University of Exeter Medical School, Hatherley Laboratories, Prince of Wales Road, Exeter, EX4 4PS, UK.
[5] MRC Laboratory of Molecular Biology (LMB), Cambridge Biomedical Campus, Francis Crick Avenue, Trumpington, Cambridge CB2 0QH, UK
[6] Centre for Gene Therapy and Regenerative Medicine, King's College London, SE1 9RT, UK
[7] Mouse Imaging Centre (MICe), Hospital for Sick Children, Toronto, Ontario M5T 3H7, Canada
[8] Comprehensive Cancer Centre, King's College London, Great Maze Pond, London SE1 1UL, UK
[9] Biomarker Research And Imaging in Neuroscience (BRAIN) Centre, Department of Neuroimaging King's College London, London, SE5 9NU, UK
[10] Bloorview Research Institute, Holland Bloorview Kids Rehabilitation Hospital, Toronto, Ontario, Canada
[11] Wellcome Centre for Integrative Neuroimaging, Nuffield Department of Clinical Neurosciences, University of Oxford, Oxford, OX3 9DU, UK
[12] Department of Basic and Clinical Neuroscience, King's College London, Maurice Wohl Clinical Neuroscience Institute, 5 Cutcombe Rd, London SE5 9RT, UK
[13] Social, Genetic and Developmental Psychiatry Centre, Institute of Psychiatry, Psychology and Neuroscience, 16 De Crespigny Park, London SE5 8AB, UK

Short title: Autism-like phenotypes in KDM5B-deficient mice

Correspondence to:

Prof. M. A. Basson
Department of Clinical and Biomedical Sciences
Hatherley Laboratories
Prince of Wales Road
Exeter, EX4 4PS
UK
m.a.basson@exeter.ac.uk

Abstract

Loss-of-function mutations in genes encoding lysine demethylases specific for trimethylated lysine 4 of histone 3 (H3K4me3) are associated with neurodevelopmental conditions, including autism spectrum disorder (ASD) and intellectual disability. To study the role of KDM5B (Lysine DeMethylase-5B)-mediated H3K4me3 demethylation, we investigated neurodevelopmental phenotypes in mice without KDM5B demethylase activity. These mice exhibited autism-like behaviours and increased brain size. H3K4me3 levels and the expression of neurodevelopmental genes were increased in the developing *Kdm5b* mutant neocortex. Increased H3K4me3 levels at the promoter and associated expression of the *Grin2d* gene was associated with increased levels of NMDAR2D protein in synaptosomes isolated from the early postnatal *Kdm5b*-deficient neocortex. Treating mice with the NMDAR antagonist memantine rescued deficits in ultrasonic vocalizations. These findings suggest that increased H3K4me3 levels and associated *Grin2d* gene upregulation disrupt brain development and function, leading to socio-communication deficits and identify a potential therapeutic target for neurodevelopmental disorders associated with KDM5B deficiency.

Teaser

Inhibitors targeting NMDA receptors may represent viable therapies for KDM5B neurodevelopmental disorders

Introduction

Mutations and variants in >50 genes encoding proteins associated with chromatin are linked to neurodevelopmental disorders (*1*). Several of these factors function as regulators of chromatin modified by histone 3 lysine 4 trimethylation (H3K4me3), a post-translational modification typically found at active gene promoters (*2, 3*). As H3K4me3 is permissive for transcription and linked to transcriptional elongation and output (*4*), mutations in genes encoding histone methyltransferases that catalyse H3K4 methylation, or in genes encoding "reader" proteins that mediate downstream effects of H3K4me3, are predicted to be associated with reduced transcription (*5, 6*). Examples include CHD8, an ATP-dependent chromatin remodeler recruited to H3K4me2/3 and KMT2A, a H3K4 methyltransferase. Mutations of the *CHD8* or *KMT2A* genes cause defined syndromes characterised by ASD with high penetrance (*7-14*). H3K4me2 levels were found to be reduced in a small set of brain samples from idiopathic ASD individuals and genetically defined ASD mouse models (*15*). Restoring normal H3K4me2 levels in these mouse models by treatment with H3K4-specific lysine demethylases rescued ASD-associated phenotypes, suggesting that the reduced H3K4me2 levels are responsible for these phenotypes (15).

Intriguingly, mutations in H3K4me3-specific demethylases of the KDM5 family are also associated with ASD (*12, 13, 16*), suggesting that increased H3K4me3 and transcriptional output could also lead to ASD. A recent forward genetic study identified recessive *Kdm5a* mutations in mice with alterations in ultrasonic vocalization (USV) emissions and nest building phenotypes and further reported evidence for social, repetitive and cognitive phenotypes in *Kdm5a*$^{-/-}$ mice (*17*). Hayek at al. further showed that individuals with recessive and heterozygous *KDM5A* mutations exhibited ASD,

developmental delay and intellectual disability. Mutations in the X-linked KDM5C gene that either disrupt its demethylase activity, or keep enzymatic activity intact, cause the intellectual disability Claes-Jenssen syndrome in males (*18, 19*). Recessive mutations in *KDM5B* cause a human syndrome associated with developmental delay, ASD, intellectual disability, hypotonia, craniofacial and limb abnormalities (*20*). In contrast to loss-of-function variants in genes like *CHD8* that are associated with ASD at high penetrance, heterozygous *KDM5B* mutations associated with ASD and developmental delay are not fully penetrant, and are often inherited from apparently unaffected parents (*13, 21-25*). Many ASD-associated missense mutations in *KDM5B* map to the JmjN, ARID and JmjC domains that form the catalytic domain of the protein, suggesting that changes in demethylase activity are associated with the neurodevelopmental phenotypes in these individuals (*21*). Two recent studies have found a significant association between *KDM5B* protein truncating variants and attention deficit hyperactivity disorder (ADHD) (*26, 27*), suggesting that *KDM5B* loss of function variants predispose to a number of neurodevelopmental disorders.

KDM5B is essential for normal development with homozygous loss-of-function mutations in mice resulting in embryonic or significant early postnatal lethality (*24, 28, 29*). Similar to Drosophila *Kdm5*, the lysine demethylase activity of KDM5B is not essential for embryonic development as a homozygous mouse model that lacks this activity is viable and fertile with only a subtle mammary gland phenotype reported to date (*29, 30*). These findings are consistent with the observation that H3K4me3 levels only become dysregulated in *Kdm5b*-deficient brain tissue after E17.5 (*28*). The reason why *Kdm5b* deficiency has little effect on H3K4me3 levels in the brain in the

mid-gestation embryo is not known, but the most likely possibility is compensation by other KDM5 family members.

In addition to mutations in genes encoding chromatin remodeling factors and synaptic proteins, de novo variants in genes encoding N-methyl-D-aspartate receptor (NMDAR) subunits have been identified in ASD probands and both reduced and elevated NMDAR activity have been implicated in ASD (*31, 32*). NMDARs are ligand-gated cation channels that mediate excitatory synaptic transmission (*33*). Increased NMDAR function during the early postnatal period (prior to P21), has been reported in specific ASD rodent models, including a *Shank2*$^{e6-7}$ mutant and valproic acid exposure model (*34, 35*). The expression of the genes encoding NMDAR subunits are developmentally regulated. For instance, *Grin2d*, encoding the NMDAR2D subunit, is not expressed in the prenatal neocortex, but is upregulated early postnatally, with peak expression at PND7, whereafter expression declines (*36*). Treatment of *Shank2*$^{e6-7}$ mutant mice at the time of NMDAR overactivity (P7-P21) with a non-competitive NMDAR antagonist, memantine (*37*), rescued the sociability phenotype (*35*). Memantine treatment of adult *IRSp53* knockout mice was also able to restore social interactions but not a hyperactivity or adult ultrasonic vocalization phenotype (*38*). The NMDAR antagonist agmatine rescued the social, hyperactivity and repetitive behavioural phenotypes in a VPA-exposed rat ASD model (*39*). Intriguingly, reduced NMDAR function has been linked to social deficits in *Shank3* mutant mice, and treatment with histone deacetylase inhibitors rescued these deficits and restored NMDAR expression and function (*40, 41*).

To test if dysregulation of the H3K4me3 demethylase activity of KDM5B is sufficient to cause ASD, we characterised mice that lack KDM5B demethylase activity (*30*). These mice were found to exhibit ASD-like behavioural phenotypes. Molecular studies revealed increased H3K4me3 levels and gene expression abnormalities in the early postnatal brain. These changes included an upregulation of the NMDAR2D subunit, encoded by the *Grin2d* gene in specific cell types. Treatment with memantine increased ultrasonic vocalization emission in pups and reduced excessive digging behaviour in adult mice, suggesting that NMDAR hyperactivation may be responsible for ASD-like behavioural phenotypes.

Results

KDM5B is a H3K4me3 demethylase in the developing neocortex

To study the function of the histone demethylase KDM5B and avoid complications due to embryonic or early postnatal lethality, we established a mouse line in which exons 2 to 4 were deleted, resulting in the truncation of the carboxyl end of the JmjN domain and deletion of the entire ARID domain (Fig. 1A). This mutation specifically disrupts the H3K4me3 demethylase activity of the protein, leaving the developmental functions of KDM5B required for embryonic development and postnatal survival intact (*29, 30*). Albert et al. have shown that *Kdm5b* deletion only affects H3K4me3 levels from late embryonic brain development (*28*), so we focussed our analysis on postnatal stages.

Homozygous *Kdm5b*$^{\Delta ARID/\Delta ARID}$ (*Kdm5b*$^{\Delta/\Delta}$) mice on a C57BL/6J background were born within expected ratios from *KDM5B*$^{+/\Delta}$ intercrosses (+/+: 31.54%; +/Δ: 46.37%; Δ/Δ: 22.07%, n=69, χ^2 test, p=0.6077) with no reduction in postnatal survival (Fig. 1B). When examined at postnatal day 12 (PND 12), homozygous mutant mice displayed decreased body weight compared to wildtype littermates, suggesting some effect on their ability to grow or thrive (Fig. 1C). Intriguingly, at this stage mutant mice exhibited increased brain-to-body weight ratios (Fig. 1D), whilst the relative size of other vital organs was not affected (Fig. 1E), suggesting specific neurodevelopmental functions for KDM5B.

To determine the effects of the ΔARID mutation on KDM5B protein in the brain, we visualised KDM5B by immunoblot in brain lysates. The shorter KDM5B ΔARID protein was detected in hippocampal and neocortical samples from PND5 control, *Kdm5b*$^{+/\Delta}$ and *Kdm5b*$^{\Delta/\Delta}$ pups, with the expected reduced molecular weight (Fig. 1F). In line with

previous results (*30*), full length KDM5B protein was reduced by 50% in the neocortex of *Kdm5b*$^{+/\Delta}$ mice and absent in *Kdm5b*$^{\Delta/\Delta}$ mice (Fig. 1F,G). Importantly, total (full-length plus ΔARID) KDM5B protein levels were reduced in the neocortex of homozygous mice compared to wildtype littermates (Fig. 1F,H). Thus, in addition to the reported lack of demethylase activity, our data suggest that the ΔARID protein is also slightly less stable than the full-length protein, although the possibility that the antibody is less efficient at detecting the mutant protein cannot be excluded.

The ΔARID protein lacks demethylase activity in in vitro assays (*30*). To determine if KDM5B functions as a H3K4me3 demethylase in the developing brain, and if steady-state H3K4me3 levels are altered in *KDM5B*$^{\Delta/\Delta}$ mice, we compared H3K4me3 levels in brain tissue from wildtype, heterozygous and homozygous mice. We detected a significant increase in H3K4me3 levels in neocortical samples from homozygous, but not heterozygous mice (Fig. 1I,J).

Autism-like behavioural phenotypes in *Kdm5b*$^{\Delta/\Delta}$ mice

To determine if a reduction in KDM5B levels and lack of KDM5B demethylase activity are sufficient to cause behavioural phenotypes in mice, we assessed socio-communicative, repetitive, anxiety and motor behaviours (Fig 2A). Both male and female animals were tested (Fig. S1), and data were combined when no significant sex differences were observed (Fig. 2). Homozygous pups emitted significantly fewer USVs upon separation from the mother (Fig. 2B). Homozygous adults exhibited no significant differences in social approach and social investigation compared to wildtype littermates in the social investigation and 3-chamber and tests, respectively (Fig. 2C,D). In the marble burying test, a measure of repetitive behaviours, mutant mice

buried marbles significantly faster than wildtype littermates, indicative of compulsive, repetitive digging behaviours (Fig. 2E). General locomotion and anxiety levels did not differ between genotypes in an open field arena (Fig. 2F and Fig. S1E,F). As further confirmation, no differences were found in the elevated plus maze test (EPM) (Fig. 2G), another test for anxiety. Homozygous mice showed reduced performance compared to wildtype animals in the accelerating rotarod task (Fig. 2H). *Kdm5b*$^{\Delta/\Delta}$ mice exhibited reduced hindlimb grip strength (Fig. 2I,J), which may have contributed to their poor performance on the rotarod test and is consistent with a report of hypotonia in an individual with recessive *KDM5B* mutations (*42*).

Structural brain anomalies associated with KDM5B deficiency

Intact brains were collected from the mice that underwent ultrasonic vocalization phenotyping (Fig. 2A). Structural magnetic resonance imaging (MRI) was performed to identify changes in absolute and relative volumes. We assessed 290 brain regions with divisions across the cortex, subcortical areas, cerebellum, brain stem, ventricular systems and fiber tracts (see Tables S1-4 for full results). A 4.2% (±1.06%) increase in brain volume was detected in homozygous mutant animals (Fig. 3A). Moreover, absolute volumes for the fiber tracts and the ventricular systems were also increased in *Kdm5b*$^{\Delta/\Delta}$ mice (6.02±0.62% and 15.23±10.47%, respectively) (Fig. 3B,C). Alterations within the fiber tracts included the anterior commissure (temporal limb) and the corticospinal tract. Mutant mice showed increases in volume across cortical areas such as the anterior olfactory nucleus, the endopiriform nucleus, the taenia tecta, the infralimbic area, the primary somatosensory area associated to the nose, and the dorsal auditory area (11.28±1.9%, 8.57±2.04%, 8.84±1.56%, 11.17±0.36%, 7.39±3.06% and 9.34±0.61% increases, respectively) (Fig. 3G and Tables S1 and S3).

Kdm5b$^{\Delta/\Delta}$ mice also showed robust increases in volume in cerebral nuclei such as the striatum (+7.52±1.52%), dorsal pallidum (+9.04±3.38%), lateral septum (+7.32±0.43%), the thalamus (+5.54±1.77%), and in the cerebellar nodular lobe (+15.67±2.07%) (Fig. 3G and Tables S1 and S3).

After correction for total brain volume, relative volumes were significantly reduced in the dentate nucleus (-6.84±0.9%) but still significantly larger in the anterior commissure of the temporal limb (+12.64±2.18%) and in the corticospinal tract (+6.16±0.68%) (Fig. 3D-F). Voxel-wise differences showed similar trends (Fig. 3G). We did not detect significant differences between wild-type and heterozygous animals in either absolute or relative volumes, although similar trends were apparent compared to homozygotes (Fig. S2 and Tables S2 and S4). Accordingly, brain volume negatively correlated with wildtype *Kdm5b* copy number (Fig. S2B-G).

KDM5B regulates the expression of neurodevelopmental genes

The increased H3K4me3 observed in the PND5 neocortex of *Kdm5b*$^{\Delta/\Delta}$ mice (Fig. 1G) is predicted to result in increased gene expression. To test this hypothesis, gene expression in *Kdm5b*$^{\Delta/\Delta}$ and wildtype PND5 neocortical and hippocampal tissues were compared by RNA sequencing (RNA-seq) (Tables S5 and S6). This analysis identified 156 differentially expressed genes (DEGs, logFoldchange >0.26; FDR<0.05) in the neocortex (Fig. 4A) and 118 DEGs in the hippocampus (Fig. 4F). The transcriptomic differences between the two genotypes were visualised in Volcano plots and heatmaps, where the majority of transcripts were upregulated in *Kdm5b*$^{\Delta/\Delta}$ mice, both in the neocortex (Fig. 4A,B) (88%) and hippocampus (Fig. 4F,G) (85%), in support of

our hypothesis. Fourty-four of the DEGs were shared between the neocortex and the hippocampus (Fig. S4, Tables S9 and S10).

Gene set enrichment analyses were performed to identify potential biological functions affected in *Kdm5b*$^{\Delta/\Delta}$ mutants. This analysis identified a significant increase in synaptic signaling processes, in both neocortical and hippocampal datasets, together with a significant overall decrease in genes related to histone complexes and RNA processing (Fig. 4E,J). A few differentially expressed genes were known SFARI ASD-associated genes (Fig. 4C,H), and ID PanelApp intellectual disability-associated genes (Fig. 4D,I) (Tables S7 and S8). These ASD/ID-associated genes included the most significantly downregulated gene, *Mcm6* (*12, 13, 43*), the downregulated gene *Slc7a3*, which encodes the Cationic amino acid transporter CAT3 (*44*), and the NMDAR subunit gene *Grin2d*, which was upregulated. We validated the upregulation of *Grin2d* and downregulation of *Mcm6* by qPCR, noting that the apparent increase in *Grin2d* levels in the neocortex was not significant in this assay (Fig. S3).

Genome-wide changes in H3K4me3

To identify genes with increased H3K4me3 levels at promoter regions and therefore most likely direct targets of KDM5B, we performed CUT&Tag-seq from PND5 neocortices (n=2 wildtype, n=2 mutant). This genome-wide analysis showed a notable increase in H3K4me3 intensity at TSSs in the *Kdm5b*$^{\Delta/\Delta}$ samples (Fig. 5A), consistent with our Western blot analysis (Fig. 1I,J). Consistent with the function of KDM5B, the most pronounced changes in H3K4me3 involved increased H3K4me3, while genes with reduced H3K4me3 showed relatively small changes (Fig. 5B and Table S10). An overlap with RNA-seq data found increased H3K4me3 at TSSs of 2 downregulated

genes, while 49 upregulated genes showed increased H3K4me3, consistent with these being most likely directly regulated by KDM5B (Table S11).

We visualized H3K4me3 changes at the promoters of three exemplary genes: upregulated *Grin2d* and *Cpne9*, and *Mcm6*, the most downregulated gene in our bulk RNA-seq experiment (Fig. 5D). H3K4me3 levels were significantly increased at both promoters of the upregulated genes (Fig. 5D, Table S10). Thus, H3K4me3 changes correlated with gene expression changes for *Grin2d and Cpne9*, suggesting that both genes are most likely direct targets of KDM5B. H3K4me3 levels at the *Mcm6* promoter were not significantly changed in *Kdm5b* mutants (Table S10), albeit that a trend for increased H3K4me3 levels were evident (Fig. 5D), suggesting that the downregulated expression of *Mcm6* is mediated via a different mechanism than direct regulation of H3K4me3.

Single nucleus RNA-seq (snRNA-seq) reveals specific cell types contributing to *Grin2d* upregulation in the *Kdm5b* mutant neocortex

As pleiotropic chromatin regulators like KDM5B are likely to perform different functions in multiple cell types in the developing brain, we performed snRNA-seq on PND5 neocortices (n=8 wildtype, n=8 mutant) (Fig. 6A). After quality control filtering, data from 21,359 wildtype nuclei and 17,098 Δ/Δ nuclei were taken forward for analysis. Both genotypes included all major cell types (Fig. 6B), each characterized by the expression of their canonical markers (Fig. S5A). We did not detect significant differences in the relative proportions of these cell types between control and mutant samples (Fig. 6C, Fig. S5B). An analysis of *Kdm5b* expression revealed the highest expression in vascular cells, intermediate progenitors, immature neurons and

astrocytes (Fig. 6D). To validate our bulk RNA-seq data and identify the cell types responsible for gene expression differences, we analyzed cell type-specific expression of the top up- and downregulated genes from the bulk RNA-seq experiment. *Cpne9* is upregulated in glutamatergic neurons (callosal projection neurons (CPN), corticofugal neurons and stellate/layer 4 cells), immature neurons and intermediate progenitors. The small fraction (<5%) of GABAergic cells expression *Cpne6* showed a converse downregulation in mutants (Fig. 6E). *Mcm6* was downregulated in all cell types examined with the largest contribution from vascular cells and intermediate progenitors and, to a lesser extent, GABAergic interneurons (Fig. 6E).

The upregulation of *Grin2d*, which encodes an NMDAR subunit (NMDAR2D), in *Kdm5b* mutants suggested a possible neurodevelopmental mechanism responsible for behavioral phenotypes. Microduplications at 19q13.33 that includes the *GRIN2D* gene (*45*), and both de novo gain- and loss-of-function mutations in GRIN2D are associated with neurodevelopmental disorders (46, 47). Bi-directional changes in NMDAR signaling have been implicated in ASD (31). An analysis of publicly available RNA-seq data *(48, 49)* confirmed that *Grin2d* expression is developmentally regulated, with expression peaking in late fetal development in humans and early postnatal development in mice (Fig. S6).

An analysis of the snRNA-seq data showed that *Grin2d* was expressed in the majority of vascular cells and intermediate progenitors (Fig. 7A), similar to *Kdm5b* (Fig. 6D). Expression levels were highest in VIP+ interneurons, followed by SST+ interneurons, intermediate progenitors and CPN L5/6 neurons, albeit that a smaller fraction of interneurons appeared to express *Grin2d* (Fig. 7A). *Grin2d* expression was

upregulated in mutant mice in GABAergic VIP neurons and all glutamatergic cell types except for stellate/layer 4 neurons. Reduced *Grin2d* expression was observed in astrocytes, oligodendrocytes, Cajal Retzius cells and intermediate progenitors in mutant samples. No evident differences were observed in vasculature or immature neurons (Fig. 7B).

Given the clear increase in *Grin2d* mRNA levels in glutamatergic cells, we next asked if the levels of NMDAR2D protein, encoded by the *Grin2d* gene, were increased in synaptosomes isolated from the PND5 neocortex of *Kdm5b*$^{\Delta/\Delta}$ mutants. NMDAR2D protein levels were quantified in purified synaptosomes and the remaining non-synaptosomal fraction. NMDAR2D levels were not changed in the non-synaptosomal fraction, but were significantly increased in synaptosomes from mutant neocortices, compared to wildtype tissue (Fig. 7C, D). This result is in line with the clear changes in *Grin2d* expression in glutamatergic neurons in mutant mice, as synaptosomal preparations tend to be enriched for excitatory synapses *(50)*. Together, these findings suggest that the increased expression of *Grin2d* results in upregulated NMDAR2D that is preferentially incorporated into synaptic NMDARs.

Treatment with an NMDAR antagonist can rescue behavioural phenotypes

Together, these observations suggested that increased NMDAR signaling during early postnatal development may underlie the behavioural phenotypes. To find direct evidence for elevated NMDAR signaling, we set out to measure AMPA:NMDA receptor ratios. However, we could not obtain reliable AMPAR responses in PND5 mice, most likely due to the preponderance of “silent” synapses at this stage of development when most synapses only contain functional NMDAR, not AMPAR *(51, 52)*. We were able

to measure AMPA:NMDA ratios at PND14, and found these to be the same in wildtype and mutant mice (Fig. S7), consistent with the possibility that elevated NMDAR2D effects are transient.

To find functional evidence that elevated NMDAR signaling in the early postnatal brain is responsible for behavioral phenotypes in *Kdm5b* mutants, we asked if pharmacological inhibition of NMDARs could rescue these phenotypes. As NMDAR inhibition might be a potential therapeutic approach to explore in our *Kdm5b*-deficient mouse model, we decided to treat mice with the NMDAR antagonist memantine, which has an acceptable safety profile in humans, can cross the blood brain barrier and has shown some promise in the treatment of epileptic encephalopathy linked to increased NMDAR (*53*). As memantine has a half-life of <4h in rodents (*54*), memantine was administered 30 min before testing, in agreement with other studies (*38, 55-58*). Memantine (5.6mg/kg) administration by intraperitoneal injection 30 min before the test significantly increased the number of ultrasonic calls emitted by *Kdm5b* mutants in response to maternal separation (repeated measures Two-way ANOVA interaction effect $F_{(4,48)}=3.520$, *p=0.0134), most notably at postnatal day 8 (Fig. 8B), the peak of USV emission (see Fig. 2B). Importantly, memantine had no significant effect on the number of USVs produced by wild-type animals (Fig. 8C), consistent with memantine targeting a mechanism responsible for the USV deficits in mutant mice.

Memantine treatment (10mg/kg) of adult mice has been shown previously to strongly suppress repetitive digging behaviour in the marble burying test in wildtype mice (*55, 56*). We reproduced these findings by finding that marble burying was almost completely abrogated in both the *Kdm5b*$^{\Delta/\Delta}$ mutant mice and wild-type littermates (Fig.

8D, E). These observations suggest that NMDAR activity is a critical requirement for repetitive digging behaviours in mice, regardless of genotype. We also found that memantine treatment reduced the motor performance of wildtype animals in the accelerating rotarod test (Fig. 8G). Memantine had no significant effect on the performance of mutant mice (Fig. 8F). These findings suggest that NMDAR antagonist treatment in the early postnatal period when *Grin2d* expression peaks and expression is elevated in *Kdm5b* mutants can rescue socio-communicative deficits. Although memantine treatment in adults can strongly suppress repetitive behaviours, these effects are not specific to *KDM5B* deficiency. Together, these observations suggest that an NMDAR-mediated mechanism is responsible for the early postnatal behavioural phenotypes in *Kdm5b* mutants.

Discussion

In this study, we characterised the neurodevelopmental phenotypes of a mouse model homozygous for a hypomorphic, demethylase-deficient allele of *Kdm5b* on a C57BL/6J genetic background. These mice exhibited socio-communicative, repetitive and motor phenotypes consistent with the association of KDM5B loss of function variants with ASD and motor stereotypies (*12, 59-61*). Steady-state H3K4me3 levels were elevated across the genome and a number of genes were differentially expressed in the early postnatal neocortex of these mice, compared to wildtype littermates. As expected for a transcriptional repressor and consistent with the increased H3K4me3 levels, the majority of differentially expressed genes were upregulated. One of these upregulated genes, *Grin2d*, encodes an NMDAR subunit implicated in neurodevelopmental disorders. We treated mice with the NMDAR antagonist, memantine, and found that this treatment ameliorated socio-communicative deficits in *Kdm5b* mutant pups. Together, our findings show that KDM5B deficiency results in neurodevelopmental phenotypes, suggest a potential mechanistic link with NMDAR gain-of-function conditions and suggest that NMDAR antagonists may represent a potential therapeutic avenue for improving socio-communicative function in individuals with *KDM5B* loss-of-function variants.

The ΔARID mouse model was engineered to delete part of the JmjN and the whole ARID domain to generate a KDM5B protein that lacks demethylase activity (*29*). A recent study confirmed that this so-called ΔARID protein lacks demethylase activity, most likely due to structural protein alterations in the catalytic Jmj domains (*30*). Here, we presented data to suggest that the ΔARID protein is also present at reduced levels in the brain compared to the wildtype, full-length protein. As previously reported,

homozygous ΔARID mice were viable (*29*), and we found no evidence for reduced viability. This contrasts with other homozygous *Kdm5b* loss-of-function mouse models that exhibited pronounced reductions in embryonic or early postnatal viability (*24, 28, 29*). Intriguingly, some homozygous null *Kdm5b* mice with an exon 7 deletion, predicted to generate a frameshift and termination mutation, survive to adulthood, and exhibited a subtle reduction in social interactions and a deficit in social memory (*24, 29*).

The initial report of de novo "likely gene disrupting" and missense variants in *KDM5B* in probands with ASD also reported similar variants in the unaffected control population (*12*). It therefore remained unclear if, and to what extent these variants contribute to neurodevelopmental phenotypes. A number of recent studies has now confirmed beyond any doubt that *KDM5B* variants are associated with these neurodevelopmental changes, but that these effects are incompletely penetrant. As a consequence, ASD-associated *KDM5B* variants are amongst the most common inherited ASD-causing variants identified to date (*13, 23*). The identification of genetic modifiers of *KDM5B* penetrance and expressivity will be of substantial interest. Our findings suggest that variants affecting the NMDAR pathway may be potent modifiers of the social phenotypes.

An improved understanding of KDM5B genotype-phenotype correlations in the context of human neurodevelopmental disorders will be of considerable interest given our findings from the demethylase-deficient mouse strain. A recessive syndrome with compound heterozygosity for two different *KDM5B* variants, which included protein-truncating, splice site and missense mutations in the JmjC domain, have been

reported (*20, 42*). It remains unclear to what extent a reduction in H3K4me3 demethylation contributes to this condition. Wang et al. reported an apparent enrichment of heterozygous missense mutations in and around the demethylase domains (JmjN, ARID and JmjC) of *KDM5B* in individuals with ASD and developmental delay (*21*), implicating demethylase activity in these conditions. However, other studies suggest that most of the likely damaging variants in *KDM5B* are found around the PHD2-PHD3 region. KDM5B interacts with other transcription factors through its PLU domain (*62*), and with HDAC4 through its N-terminal PHD regions (*63*). Further studies are necessary to decipher the potential impact of different *KDM5B* variants on specific mechanisms, including those that may be independent from its demethylase activity. Based on our findings, we propose that variants altering the demethylase activity of KDM5B would primarily affect neurodevelopment postnatally (e.g. via NMDAR signaling), while demethylase-independent variants may affect developmental processes such as neuronal specification and differentiation in the early embryo.

Human patients carrying *KDM5B* variants display a varying degree of brain structural alterations, ranging from a normal MRI to agenesis of corpus callosum, cerebellar vermis alterations and megalencephaly (*20, 24*). Notably, one patient showed megalencephaly (*24*), in line with the general increase in absolute brain volumes observed in our *Kdm5b*$^{\Delta/\Delta}$ model. We found increased absolute and relative volumes in fiber tracts such as the corticospinal tract and the anterior commissure. We did not observe alterations specific to the corpus callosum, whereas four individuals with recessive *KDM5B* variants have shown agenesis of the corpus callosum (*42*). This discrepancy suggests that corpus callosum agenesis is not caused by alterations in

the demethylase activity of KDM5B, but other, independent KDM5B functions, although genetic background effects are also possible. Interestingly, three individuals with recessive *KDM5B* variants exhibited altered/unsteady gait (*24*). This phenotype could be related to the structural changes we observe in the cerebellum in *Kdm5b*$^{\Delta/\Delta}$ animals. The thalamus and brain stem, two crucial areas controlling posture and gait, also showed increased absolute volumes in *Kdm5b*$^{\Delta/\Delta}$ homozygous mice. The aberrant size of the striatum is in line with the reduced performance of *Kdm5b*$^{\Delta/\Delta}$ mice in the accelerating rotarod task (*64*). De novo, likely gene disrupting variants in *KDM5B* have also been linked to primary motor stereotypies, another phenotype associated with alterations in the cerebellum (*65*) and cortico-striatal-thalamo-cortical pathways (*61, 66-68*). Abnormalities in these brain regions and pathways could underlie the repetitive behaviours observed in *Kdm5b*$^{\Delta/\Delta}$ mice. Further work, by for example comparing neuronal activation during USVs in wildtype and mutant pups, are necessary to identify the regional and cell type abnormalities ultimately responsible for the behavioral phenotypes.

Chromatin modifiers and remodelers typically regulate hundreds of gene loci throughout the genome, and function in multiple cell types and at different stages of development. For instance, in the case of CHD8, many ASD-associated genes are dysregulated in the *Chd8*-deficient brain, making it difficult to determine the exact downstream genes responsible for neurodevelopmental phenotypes (*69-74*). Indeed, our snRNA-seq analysis suggests that KDM5B functions in multiple cell types in the developing postnatal brain, including neuronal progenitors, excitatory and inhibitory neurons and vascular cells. Our H3K4me3 CUT&Tag-seq experiment identified potential direct targets of KDM5B in the PND5 neocortex, including *Grin2d*. However,

attempts to directly demonstrate KDM5B recruitment to the *Grin2d* promoter by Chromatin Immunoprecipitation were unsuccessful due to the quality of commercially available antibodies.

Given the potential complexities of KDM5B function in the developing brain, we were surprised to find that treatment with an NMDAR antagonist was sufficient to improve some for the ASD-associated behavioural phenotypes in *Kdm5b* mutants. Memantine is a non-competitive antagonist of NMDARs with low affinity and rapid kinetics (*75*). This treatment presumably normalises an abnormal gain in NMDAR function due to *Grin2d* upregulation in the early postnatal brain. *Grin2d* expression in rodents starts at late embryonic stages, peaking at PND7 (*76*). In the hippocampus NMDAR2D-containing receptors mediate synaptic transmission in interneurons(*77*) and they constrain short-term and long-term potentiation in area CA1 (*78*). Our attempts to measure AMPA:NMDA ratios in PND5 hippocampus were unsuccessful due to the preponderance of “silent” synapses that lack AMPAR in the PND7 neocortex (*51, 52*). Further work is therefore required to determine the exact mechanism whereby *Grin2d* overexpression and memantine treatment affect socio-communicative behaviours in the mouse model.

In humans, gain-of-function mutations in the NMDAR subunit gene *GRIN2D* are associated with GRIN2D-related developmental and epileptic encephalopathy, a condition associated with developmental delay, intractable seizures, abnormal muscle tone, movement disorders and ASD (*46, 79-81*). NMDAR antagonists such as memantine and ketamine have proven therapeutically useful for treatment of epileptic encephalopathies associated with increased NMDAR function (*46*). In addition to

hypotonia and ASD, two individuals carrying *KDM5B* variants show epileptic spasms and generalized seizures (*24, 82*). Future studies assessing the effects of different *Kdm5b* loss-of-function variants on excitatory neurotransmission will be of interest, especially if these can be combined with NMDAR antagonist treatment.

Memantine treatment has been evaluated in individuals with ASD, with varied effects, not surprising given that both increased and reduced NMDAR function has been implicated in ASD (*31, 32, 83-87*). The present study, together with studies on *Shank2*-deficient and VPA rodent models (*35, 39*), suggest that treatment with NMDAR antagonists is likely to benefit individuals where symptoms are caused by increased NMDAR function.

In addition to *Grin2d*, the other differentially-expressed ASD-associated gene worth noting is *Mcm6*. *Mcm6* was the most downregulated gene in *Kdm5b* mutants. De novo *MCM6* variants were first detected in ASD probands by Iossifov et al. (*12*), with further reports by Takata et al. (*43*). Subsequently, missense mutations in *MCM6* were associated with neurodevelopmental phenotypes that include ASD, delayed speech development and epilepsy by Smits et al. (*88*).(*88*). MCM6 is important for primary ciliogenesis and cell proliferation (*88, 89*), two crucial processes during brain development. (*90*).

Limitations of our study include the difficulty in distinguishing between the contribution of H3K4me3 demethylase deficiency or reduced protein levels on the observed phenotypes. The *Kdm5b*$^{\Delta ARID}$ allele represents a hypomorphic allele that lacks demethylase activity as well as an apparent reduction in steady-state protein levels. It

is difficult to distinguish between effects from the reduction in KDM5B protein levels and the lack of demethylase activity. Regardless, we do find a robust upregulation of steady-state H3K4me3 levels in the neocortex at the promoters of upregulated genes, indicating that H3K4me3 demethylase activity is indeed affected in these mice. Although we were unable to directly measure changes in NMDAR signaling at early postnatal stages due to technical limitations, our treatment studies with memantine supports the idea that increased NMDAR signaling is responsible for the USV deficits. Future work using more selective NMDAR antagonists and genetic rescue experiments are needed to further support our model and assess the translational potential of targeting NMDAR signaling in the context of KDM5B neurodevelopmental disorders.

In conclusion, we have found that a deficiency in the KDM5B demethylase results in ASD-associated behavioural phenotypes in mice. *KDM5B* deficiency was associated with increased levels of H3K4me3, demonstrating that KDM5B functions as a H3K4me3 demethylase in the developing brain. These alterations affected gene expression, with the majority of differentially expressed genes upregulated, confirming that KDM5B acts primarily as a transcriptional repressor. Finally, we provide evidence to suggest that abnormal elevation of NMDAR2D-containing NMDAR signaling in the postnatal brain, is responsible for the socio-communicative deficits in these mice. These observations functionally link *KDM5B* deficiency with childhood neurodevelopmental disorders caused by NMDAR gain of function mutations and suggest a potential therapy to alleviate some of the behavioural dysfunction associated with *KDM5B* deficiency.

Materials and Methods

Animals

The *Kdm5b*$^{\Delta ARID}$ mouse line has been described (*29*). In this mouse line *Kdm5b* exons 2, 3 and 4 were removed, leading to the deletion of the entire ARID domain and the truncation of the carboxyl end of the JmJ domain. Mice were maintained in a C57BL/6J background, and experimental animals were produced by *Kdm5b*$^{+/\Delta ARID}$ x *Kdm5b*$^{+/\Delta ARID}$ intercrosses. Animals were housed in ventilated cages (37x20x16cm, Techniplas UK Ltd, Leicester, UK) with ad libitum access to water and food (Labdiet PIcolab rodent irradiated, #5R53) and kept at 19–22°C and 40–60% humidity, under a 12:12-h light/dark cycle. The cages contained sawdust (Lignocel wood fiber) and nesting material. A maximum of five animals were housed in the same cage. Our study examined male and female animals, and similar findings are reported for both sexes. All animal procedures were approved by King's College London AWERB and the UK Home Office (Home Office Project licences P8DC5B496 and PP6246123).

Genotyping of mice

Genotyping was performed by extracting genomic DNA from ear notches using Proteinase K digestion or the HotSHOT method (*91*) The following primer pairs to detect the WT and the mutant alleles were used: WT forward 5'-CCTTAGACGCAGACAGCACA-3', WT reverse 5'- CGTGTTTGGGCCTAAATGTC-3', KDM5B-ΔARID forward 5'- TGCTCCTGCCGAGAAAGTATCC-3' and KDM5B-ΔARID reverse 5'- CCACCCCCCAGAATAGAATGA-3'. Thermal cycles for the genotyping reactions were as follows: 95°C, 2 min; 35x (95°C, 15 sec; 64°C, 15 sec; 72°C, 15 sec); 72°C, 12min.

Western blots

KDM5B and Histone blots

Brain cortices and hippocampi were dissected from PND5 pups and whole cell protein prepared by lysing in 8M urea, 1% CHAPS, 50mM Tris (pH 7.9) lysis buffer containing protease inhibitors. Samples were rotated for 30min at 4°C and then centrifuged for 60min to remove DNA. Supernatant was stored at -80°C. All reagents and equipment were from BioRad unless stated otherwise. Samples were prepared with Laemmli buffer containing 10% β-mercaptoethanol and resolved with Mini-PROTEAN pre-cast polyacrylamide gels (7.5% and 4-15% gels to analyse proteins with high and medium/low molecular weights, respectively) and Tris/Glycine/SDS buffer. Proteins were transferred to a nitrocellulose membrane with the TransBlot turbo system. Membranes were blocked with 5% non-fat dry milk (Cell Signaling Technologies) or 5% BSA (Sigma) diluted in Tris-buffered saline containing 0.1% Tween-20 (TBS-T), followed by incubation overnight at 4°C with primary antibodies diluted in 5% BSA in TBS-T. Membranes were washed 3x10min in TBS-T before incubation for 1h at room temperature with secondary antibodies diluted in TBS-T containing 5% non-fat dry milk. After washing 3x10min in TBS-T, proteins were detected with Clarity ECL reagent and membranes were imaged using the Chemidoc system. Densitometric analyses were performed with ImageJ software (NIH). The following antibodies were used (1:1000 dilution unless stated otherwise): anti-KDM5B (Abcam, #181089), anti-H3K4me3 (Cell Signaling Technologies, #9751), anti-total H3 (Cell Signaling Technologies, #9715), HSP90 (Santa Cruz Biotechnologies, sc13119), actin (1:5000, Abcam, #ab8227), goat anti-rabbit and anti-mouse HRP secondary antibodies (1:5000; Thermo Fisher Scientific, #31460 and Proteintech, #SA00001-1, respectively). Uncropped western blot images are shown in Fig. S8.

NMDAR2D western blots

Brain cortices were dissected from postnatal day 5 pups and synaptosomes were isolated using Syn-PER™ Synaptic Protein Extraction Reagent (ThermoFisher) following the manufacturer's protocol. The synaptosome pellet was resuspended in RIPA buffer containing protease inhibitors and the protein concentration was quantified using a BCA assay (ThermoFisher). Laemmli buffer (Bio-rad) with DDT was added to 15µg of each sample and loaded into a 4–20% precast polyacrylamide gel (Bio-Rad, 4561095). The gel was electrophoresed for 10 minutes at 50V then 1 hour at 120V in Tris-Glycine SDS buffer (Bio-rad). The gel and nitrocellulose membrane were then equilibrised in transfer buffer (Bio-Rad) for 10 minutes before being transferred for 1 hour at 80V in the transfer buffer. The membranes were stained using Ponceau S (Merck) to check for protein transfer and blocked in PBS-T containing 5% non-fat milk buffer. The membrane was incubated with the primary antibodies overnight at 4 °C, and then repeatedly washed with PBS-T before incubation in secondary antibodies for GRIN2D (Merck, MAB5578, 1:500) and B-actin (Merck, A5316, 1:5000) overnight at 4 °C. The membranes were repeatedly washed with PBS-T before incubating them in Dylight™ 800 secondary antibody (ThermoFisher, SA5-10164, 1:5000) for 1 hour in the dark at room temperature. The membranes were then washed three times and imaged and analysed on the LICOR Odyessey CLx machine. Uncropped full scans of the western blot membranes can be found in Fig. S8.

Behaviour

Different batches of mice were used for recording pup ultrasonic vocalizations (USVs), for adult behaviour testing and for the treatment with memantine (see Fig 2A and Fig

8C). Adult tests were carried out in the following order: open field, elevated plus maze, reciprocal social tests, marble burying, 3 chamber social approach, and rotarod as previously described (*69, 71*). Behavioural experiments were conducted between 8:00 and 18:30 under standard room lighting conditions unless stated otherwise. Cages were changed every other week but never less than 24h before the day of testing. Behaviours were tracked using Ethovision (Noldus Information Technologies bv, Wageningen, The Netherlands). After each trial of a specific test, boli and urine were removed, and the test area was cleaned with 1% Anistel® solution (high level surface disinfectant, Trisel Solution Ltd, Cambridgeshire, UK) to remove any odours. The experiments were blinded and randomized by blocks of mice. Littermates were used as controls with multiple litters examined per experiment.

Ultrasonic vocalizations (USVs).

Ultrasonic vocalizations (USVs) were recorded in pups across 3-minute sessions in response to social separation from the mother and siblings at postnatal days (PND) 2, 4, 6, 8 and 12 as described (*92*). The tattooing for early identification of the mice was carried out on PND 2. Tattooing (Animal tattoo ink green paste, Ketchum #KI1471) for identification was carried out by inserting the ink subcutaneously through a 0.3 mm hypodermic needle into the center of the paw. Tattooing was carried out at PND2 in the experiment described in Figure 2, and at PND1 for the rescue experiment. USV testing as in Fig.2 was performed on a batch of 22 mice (Males: 3 WT and 6 mutant; Females: 7 WT and 6 mutant). The experiment included in Fig. 8 was performed on a batch of 15 mice (4 male and 3 female saline and 5 male 2 female memantine). During testing, each pup was transferred from its homecage to an empty glass container in a sound-attenuating box placed in a different room. Lights were turned off during the USVs recording. An Ultrasound Microphone (Avisoft UltraSoundGate condenser

microphone capsule CM16, Avisoft Bioacoustics, Berlin, Germany), sensitive to frequencies of 10 to 180 kHz, was placed through a hole in the middle of the cover of the sound-attenuating box, about 20 cm above the pup in its glass's container. USVs were recorded using the Avisoft Recorder software (Version 3.2). The glass container was cleaned with 10% ethanol between pups and with 70% ethanol between litters. For acoustical analysis, recordings were transferred to Avisoft SASLab Pro (Version 4.40) and a fast Fourier transformation (FFT) was conducted. Spectrograms were generated at a frequency resolution of 488 Hz and a time resolution of 1 ms.

Memantine treatment

A memantine (Cayman Chemical Company, #14184) solution was prepared fresh in saline (0.56mg/ml for early postnatal and 1mg/ml for adult mice) each day. 10µl/g of saline or memantine solution were administered intraperitoneally 30 minutes before recording USVs or running the marble burying and accelerating rotarod tests. Doses were 5.6 mg/kg for USVs (*93*) and 10 mg/kg for the marble burying and accelerating rotarod tests (*55, 56*).

MRI

Perfusions

Mice were anesthetized with pentobarbital and intracardially perfused with 30mL of 0.1M PBS containing 0.05 U/mL heparin (Sigma) and 2mM ProHance (Bracco Diagnostics, a Gadolinium contrast agent) followed by 30 mL of 4% paraformaldehyde (PFA) containing 2mM ProHance (*69, 94*).(*69, 94*). Perfusions were performed with a minipump at a rate of approximately 1 mL/min. After perfusion, mice were decapitated and the skin, lower jaw, ears, and the cartilaginous nose tip were removed. The brain

and remaining skull structures were incubated in 4% PFA + 2mM ProHance overnight at 4°C then transferred to 0.1M PBS containing 2mM ProHance and 0.02% sodium azide for at least 1 month prior to MRI scanning (*95*) (*95*)

Magnetic Resonance Imaging – Ex Vivo

A 7-Tesla 306 mm horizontal bore magnet (BioSpec 70/30 USR, Bruker, Ettlingen, Germany) with a ParaVision 6.0.1 console was used to image brains in skulls. Eight samples were imaged in parallel using a custom-built 8-coil solenoid array. To acquire anatomical images, the following scan parameters were used: T2-weighted 3D fast spin echo (FSE) sequence with a cylindrical acquisition of k-space, TR/TE/ETL = 350 ms/12 ms/6, TEeff = 30ms, four effective averages, FOV/matrix-size = 20.2 × 20.2 × 25.2 mm / 504 × 504 × 630, total-imaging-time = 13.2 h. The resulting anatomical images had an isotropic resolution of 40µm voxels.

Imaging Registration and Analysis

Image registration is necessary for quantifying the anatomical differences across images. The registration consisted of both linear (rigid then affine) transformations and non-linear transformations. These registrations were performed with a combination of mni_autoreg tools (Collins 1994) and ANTS (advanced normalization tools) (*96*) After registration, all scans were resampled with the appropriate transform and averaged to create a population atlas representing the average anatomy of the study sample. The result of these registrations were deformation fields that transform images to a consensus average. Therefore, these deformations fields quantify anatomical differences between images. As detailed in previous studies (*97, 98*), the Jacobian determinants of the deformation fields were computed and analyzed to measure the volume differences between subjects at every voxel. A pre-existing classified MRI

atlas was warped onto the population atlas (containing 282 different segmented structures encompassing cortical lobes, large white matter structures such as the corpus callosum, ventricles, cerebellum, brain stem, and olfactory bulbs to compute the volume of brain structures in all the input images (*99-103*).(*99-103*). A linear model with a genotype predictor was used to assess significance. The model was either fit to the volume of every structure independently (structure-wise statistics) of fit to every voxel independently (voxel-wise statistics), and multiple comparisons in this study were controlled for using the False Discovery Rate (*104*).

RNA sequencing

Total RNA was prepared as described (*69*). RNA quality was analysed using Agilent Total RNA 6000 Pico on a Bioanalyser (Agilent, 2100). Pair-end sequencing (150bp read length) was performed on the Illumina HiSeq 6000 platform. Further data analyses were performed using the Galaxy Europe server (https://usegalaxy.eu). Quality of the raw data was checked using FastQC version 0.11.9. Reads were aligned to the mouse genome (mm10) using RNA STAR Galaxy Version 2.7.8a, and aligned reads were counted using FeatureCounts Galaxy version 2.0.1. Differential expression analyses were performed using DESeq2 Galaxy version 2.11.40.7. Heatmaps were generated with the R package pheatmap. Volcano plots were generated in GraphPad Prism 9.4.1. (*105*). The criteria to select differentially expressed genes (DEGs) were: FDR < 0.05 and |log2FoldChange| >0.263. Gene Set Enrichment Analyses (GSEA) were performed on R with Clusterprofiler as described in https://learn.gencore.bio.nyu.edu/rna-seq-analysis/gene-set-enrichment-analysis (accessed September 2024). Venn diagrams were created to show the extent of overlap between heterozygous and homozygous DEGs (FDR<0.05), and ASD-

associated genes obtained from the SFARI human Gene database (https://gene.sfari.org/database/human-gene/; accessed October 2025) or ID-associated genes obtained from the Genomics England PanelApp Intelectual disability database (https://panelapp.genomicsengland.co.uk/panels/285/, version 4.42, accessed December 2022). FastQC version 0.11.9. Reads were aligned to the mouse genome (mm10) using RNA STAR Galaxy Version 2.7.8a, and aligned reads were counted using FeatureCounts Galaxy version 2.0.1. Differential expression analyses were performed using DESeq2 Galaxy version 2.11.40.7. Heatmaps were generated with the R package pheatmap. Volcano plots were generated in GraphPad Prism 9.4.1. (*105*). The criteria to select differentially expressed genes (DEGs) were: FDR < 0.05 and log2FoldChange >0.263. Gene Set Enrichment Analyses (GSEA) were performed on R with Clusterprofiler as described in https://learn.gencore.bio.nyu.edu/rna-seq-analysis/gene-set-enrichment-analysis (accessed September 2024). Venn diagrams were created to show the extent of overlap between heterozygous and homozygous DEGs (FDR<0.05), and ASD-associated genes obtained from the SFARI human Gene database (https://gene.sfari.org/database/human-gene/; accessed October 2025) or ID-associated genes obtained from the Genomics England PanelApp Intelectual disability database (https://panelapp.genomicsengland.co.uk/panels/285/, version 4.42, accessed December 2022).

Nuclei isolation for CUT&Tag and snRNA-seq

Nuclei were isolated from the cortex of PND 5 pupslby incubating tissue for 15 minutes on ice in lysis buffer (10mM Tris-HCL (pH 7.4), 10mM NaCl, 3mM $MgCl_2$, 0.1% NP-40 substitute). Tissue was mechanically homogenised with a 27g needle prior to layering

on top of 1.8M sucrose solution. 1.7μM DTT was added to the sucrose solution for snRNA-seq nuclear extractions. Samples were centrifuged at 13000xg for 45 minutes at 4°C. The resulting nuclear pellet was washed and resuspended in 2% BSA in PBS. Extracted nuclei were counted manually and checked for quality using trypan blue. For snRNA-seq, 200U Ribolock RNase inhibitor (Thermo) was added to lysis buffer, wash buffer and resuspension buffer.

CUT&Tag-seq

CUT&Tag was performed using the EpiCypher CUTANA CUT&Tag kit as per manufacturer's instructions (Epicypher, v2). 100,000 nuclei, previously stored in BAMBANKER™ at -80°C were used per reaction. In short, ConA beads were activated and bound to the isolated nuclei. 2 μL of stock K-MetStat Panel (19-1002, EpiCypher) was added to each reaction prior to addition of the antibodies. 0.5 μg of anti-H3K4me3 (13-0060, EpiCypher) or rabbit IgG negative control (13-0042, Epicypher) primary antibodies were added to each reaction and incubated on a nutator at 4°C overnight. Nuclear slurry was incubated with anti-rabbit secondary antibody (13-0047, EpiCypher) at RT for 30 minutes. Tagmentation was carried out for 1 hour at 37°C. Libraries were prepared by PCR with a unique pair of i5 and i7 indexing primers with the following parameters: 58°C, 5 minutes; 72°C, 5 minutes; 98°C, 45 seconds; 98°C, 15 seconds, 60°C, 10 seconds, 16 cycles; 72°C, 1 minute; 4°C hold. Library quality was assessed using the Tapestation (Agilent) with D1000 screentape and reagents. Libraries were quantified using the Qubit fluorometer with 1X dsDNA HS assay kit. Paired end (150bp) sequencing was performed on the Illumina NovaSeq X.

The workflow for CUT&Tag-seq data analysis was broadly performed using an adapted nf-core CUT&RUN Nextflow pipeline (*106, 107*). In brief, FastQ files were first

checked for sequencing quality using FastQC followed by trimming of adapter and low-quality sequences by Trim Galore! (version 0.6.5). Paired-end reads were aligned to the GRCm38 (mm10) genome using Bowtie2 (version 2.3.5.1) (*108*). Samtools (version 1.22.1) (*109*) was then used to sort and index BAM files, followed by marking of duplicate reads by picard (version 3.4.0). BedGraph files were generated using bedtools (2.31.0) and bigWig files were generated using bedGraphToBigWig (version 4.8.2) and visualised on the Integrative Genomics Viewer (IGV). Peak calling was performed either using MACS2 (version 2.2.9.1) or SEACR (version 1.3) (*110*) then merged to generate consensus peaks using bedTools. To spike-in normalise files for analysis and visualisation, deepTools (version 3.5.6) (*111*) was used to apply scaling factors calculated from SNAP-CUTANA K-MetStat Panel spike-ins. A scaling factor was calculated for each sample by dividing the percentage of total GRCm38-aligned reads by the percentage of total reads taken up by spike-in barcodes - this scaling factor was then applied to each sample. Following this, deepTools computeMatrix was then used to determine enrichment around gene transcription start sites (TSS) and visualised using plotHeatmap. Comparisons of H3K4me3 enrichment at gene TSS between samples was performed using diffbind (version 3.21) using windows of +/- 1kb around the TSS.

Parse sequencing

Neocortical brain samples from 8 wild-type and 8 mutant mice were dissected out and stored (-80°C) until sample processing for nuclei isolation. Isolated nuclei were immediately fixed using the Evercode Fixation kit (Parse Biosciences). Sequencing libraries were generated using the Evercode WT kit (chemistry version 3, Parse Bioscience). Paired end sequencing (150bp) was performed using the Illumina

NovaSeq-X. Raw sequencing reads were processed with the Trailmaker™ pipeline (cloud-based data processing platform from Parse Biosciences) using default settings in order to demultiplex sub-libraries, align reads to the GRCm39 reference genome, and produce cell-by-gene count matrices. Downstream analyses were completed with Scanpy (v.1.11.0). Quality control was performed by using standard parameters based on guidelines published previously (*112*). Briefly, we filtered out cells expressing a low or too high number of genes and total transcripts counts as well as those with a high mitochondrial proportion. We further used Scrublet (pp.scrublet() function) to remove doublets (*113*). Data was then normalized and log transformed using Scanpy's pp.normalize_total() and pp.log1p() functions. Log transformed counts were then used to calculate Highly Variable Genes. Integration was performed using Scanpy's external pp.harmony_integrate() function using the different samples as a covariate. We then used harmony integrated principal components analysis (PCA) for dimension reduction, and unsupervised Leiden clustering of the data with a final resolution of 0.5 to find clusters. To visualize the data we used UMAP. Cluster annotation was performed manually based on differentially expressed genes in each cluster and previous literature (*114, 115*).

Statistics

Data are reported as mean ± SEM. Graphs show individual data points. Normal distribution was tested with d'Agostino and Pearson omnibus, Shapiro-Wilk and Kolmogorov-Smirnov normality tests. If the test was passed, statistical analysis was performed using parametric statistical analyses. Before pairs of comparisons, we performed the F test to compare variances. Statistical analyses were performed using the unpaired two-sided Student-s t test and the three- and two-way ANOVA. Only

when the interaction effect was significant ($p<0.05$) was these followed with the appropriate post hoc tests as indicated in the figure legends. T test with Welch's correction was applied when variances were unequal. Significant p values ($p<0.05$) are reported in the results section and/or figure legends provide details of relevant statistical parameters, including group sizes. Statistical analyses were performed with GraphPad Prism (version 9.4.1). Researchers were blinded and in vivo studies were randomized by blocks of animals.

References

1. C. F. Wright, P. Campbell, R. Y. Eberhardt, S. Aitken, D. Perrett, S. Brent, P. Danecek, E. J. Gardner, V. K. Chundru, S. J. Lindsay, K. Andrews, J. Hampstead, J. Kaplanis, K. E. Samocha, A. Middleton, J. Foreman, R. J. Hobson, M. J. Parker, H. C. Martin, D. R. FitzPatrick, M. E. Hurles, H. V. Firth, D. D. D. Study, Genomic Diagnosis of Rare Pediatric Disease in the United Kingdom and Ireland. *The New England journal of medicine*, (2023).
2. S. M. Lauberth, T. Nakayama, X. Wu, A. L. Ferris, Z. Tang, S. H. Hughes, R. G. Roeder, H3K4me3 interactions with TAF3 regulate preinitiation complex assembly and selective gene activation. *Cell* **152**, 1021-1036 (2013).
3. M. Vermeulen, H. T. Timmers, Grasping trimethylation of histone H3 at lysine 4. *Epigenomics* **2**, 395-406 (2010).
4. H. Wang, Z. Fan, P. V. Shliaha, M. Miele, R. C. Hendrickson, X. Jiang, K. Helin, H3K4me3 regulates RNA polymerase II promoter-proximal pause-release. *Nature* **615**, 339-348 (2023).
5. J. Cotney, R. A. Muhle, S. J. Sanders, L. Liu, A. J. Willsey, W. Niu, W. Liu, L. Klei, J. Lei, J. Yin, S. K. Reilly, A. T. Tebbenkamp, C. Bichsel, M. Pletikos, N. Sestan, K. Roeder, M. W. State, B. Devlin, J. P. Noonan, The autism-associated chromatin modifier CHD8 regulates other autism risk genes during human neurodevelopment. *Nature communications* **6**, 6404 (2015).
6. A. Sugathan, M. Biagioli, C. Golzio, S. Erdin, I. Blumenthal, P. Manavalan, A. Ragavendran, H. Brand, D. Lucente, J. Miles, S. D. Sheridan, A. Stortchevoi, M. Kellis, S. J. Haggarty, N. Katsanis, J. F. Gusella, M. E. Talkowski, CHD8 regulates neurodevelopmental pathways associated with autism spectrum disorder in neural progenitors. *Proc Natl Acad Sci U S A* **111**, E4468-4477 (2014).
7. R. Bernier, C. Golzio, B. Xiong, H. A. Stessman, B. P. Coe, O. Penn, K. Witherspoon, J. Gerdts, C. Baker, A. T. Vulto-van Silfhout, J. H. Schuurs-Hoeijmakers, M. Fichera, P. Bosco, S. Buono, A. Alberti, P. Failla, H. Peeters, J. Steyaert, L. E. Vissers, L. Francescatto, H. C. Mefford, J. A. Rosenfeld, T. Bakken, B. J. O'Roak, M. Pawlus, R. Moon, J. Shendure, D. G. Amaral, E. Lein, J. Rankin, C. Romano, B. B. de Vries, N. Katsanis, E. E. Eichler, Disruptive CHD8 mutations define a subtype of autism early in development. *Cell* **158**, 263-276 (2014).
8. N. Krumm, B. J. O'Roak, J. Shendure, E. E. Eichler, A de novo convergence of autism genetics and molecular neuroscience. *Trends Neurosci* **37**, 95-105 (2014).
9. B. M. Neale, Y. Kou, L. Liu, A. Ma'ayan, K. E. Samocha, A. Sabo, C. F. Lin, C. Stevens, L. S. Wang, V. Makarov, P. Polak, S. Yoon, J. Maguire, E. L. Crawford, N. G. Campbell, E. T. Geller, O. Valladares, C. Schafer, H. Liu, T. Zhao, G. Cai, J. Lihm, R. Dannenfelser, O. Jabado, Z. Peralta, U. Nagaswamy, D. Muzny, J. G. Reid, I. Newsham, Y. Wu, L. Lewis, Y. Han, B. F. Voight, E. Lim, E. Rossin, A. Kirby, J. Flannick, M. Fromer, K. Shakir, T. Fennell, K. Garimella, E. Banks, R. Poplin, S. Gabriel, M. DePristo, J. R. Wimbish, B. E. Boone, S. E. Levy, C. Betancur, S. Sunyaev, E. Boerwinkle, J. D. Buxbaum, E. H. Cook, Jr., B. Devlin, R. A. Gibbs, K. Roeder, G. D. Schellenberg, J. S. Sutcliffe, M. J. Daly, Patterns and rates of exonic de novo mutations in autism spectrum disorders. *Nature* **485**, 242-245 (2012).
10. B. J. O'Roak, L. Vives, W. Fu, J. D. Egertson, I. B. Stanaway, I. G. Phelps, G. Carvill, A. Kumar, C. Lee, K. Ankenman, J. Munson, J. B. Hiatt, E. H. Turner, R. Levy, D. R. O'Day, N. Krumm, B. P. Coe, B. K. Martin, E. Borenstein, D. A. Nickerson, H. C. Mefford, D.

Doherty, J. M. Akey, R. Bernier, E. E. Eichler, J. Shendure, Multiplex targeted sequencing identifies recurrently mutated genes in autism spectrum disorders. *Science* **338**, 1619-1622 (2012).

11. B. J. O'Roak, L. Vives, S. Girirajan, E. Karakoc, N. Krumm, B. P. Coe, R. Levy, A. Ko, C. Lee, J. D. Smith, E. H. Turner, I. B. Stanaway, B. Vernot, M. Malig, C. Baker, B. Reilly, J. M. Akey, E. Borenstein, M. J. Rieder, D. A. Nickerson, R. Bernier, J. Shendure, E. E. Eichler, Sporadic autism exomes reveal a highly interconnected protein network of de novo mutations. *Nature* **485**, 246-250 (2012).
12. I. Iossifov, B. J. O'Roak, S. J. Sanders, M. Ronemus, N. Krumm, D. Levy, H. A. Stessman, K. T. Witherspoon, L. Vives, K. E. Patterson, J. D. Smith, B. Paeper, D. A. Nickerson, J. Dea, S. Dong, L. E. Gonzalez, J. D. Mandell, S. M. Mane, M. T. Murtha, C. A. Sullivan, M. F. Walker, Z. Waqar, L. Wei, A. J. Willsey, B. Yamrom, Y. H. Lee, E. Grabowska, E. Dalkic, Z. Wang, S. Marks, P. Andrews, A. Leotta, J. Kendall, I. Hakker, J. Rosenbaum, B. Ma, L. Rodgers, J. Troge, G. Narzisi, S. Yoon, M. C. Schatz, K. Ye, W. R. McCombie, J. Shendure, E. E. Eichler, M. W. State, M. Wigler, The contribution of de novo coding mutations to autism spectrum disorder. *Nature* **515**, 216-221 (2014).
13. X. Zhou, P. Feliciano, C. Shu, T. Wang, I. Astrovskaya, J. B. Hall, J. U. Obiajulu, J. R. Wright, S. C. Murali, S. X. Xu, L. Brueggeman, T. R. Thomas, O. Marchenko, C. Fleisch, S. D. Barns, L. G. Snyder, B. Han, T. S. Chang, T. N. Turner, W. T. Harvey, A. Nishida, B. J. O'Roak, D. H. Geschwind, S. Consortium, J. J. Michaelson, N. Volfovsky, E. E. Eichler, Y. Shen, W. K. Chung, Integrating de novo and inherited variants in 42,607 autism cases identifies mutations in new moderate-risk genes. *Nat Genet* **54**, 1305-1319 (2022).
14. W. D. Jones, D. Dafou, M. McEntagart, W. J. Woollard, F. V. Elmslie, M. Holder-Espinasse, M. Irving, A. K. Saggar, S. Smithson, R. C. Trembath, C. Deshpande, M. A. Simpson, De novo mutations in MLL cause Wiedemann-Steiner syndrome. *Am J Hum Genet* **91**, 358-364 (2012).
15. M. Rapanelli, J. B. Williams, K. Ma, F. Yang, P. Zhong, R. Patel, M. Kumar, L. Qin, B. Rein, Z. J. Wang, B. Kassim, B. Javidfar, L. Couto, S. Akbarian, Z. Yan, Targeting histone demethylase LSD1 for treatment of deficits in autism mouse models. *Mol Psychiatry* **27**, 3355-3366 (2022).
16. T. Wang, C. E. Kim, T. E. Bakken, M. A. Gillentine, B. Henning, Y. Mao, C. Gilissen, T. S. consortium, T. J. Nowakowski, E. E. Eichler, Integrated gene analyses of de novo mutations from 46,612 trios with autism and developmental disorders. *BioRxiv*, (2021).
17. L. El Hayek, I. O. Tuncay, N. Nijem, J. Russell, S. Ludwig, K. Kaur, X. Li, P. Anderton, M. Tang, A. Gerard, A. Heinze, P. Zacher, H. S. Alsaif, A. Rad, K. Hassanpour, M. R. Abbaszadegan, C. Washington, B. R. DuPont, R. J. Louie, C. Study, M. Couse, M. Faden, R. C. Rogers, R. Abou Jamra, E. R. Elias, R. Maroofian, H. Houlden, A. Lehman, B. Beutler, M. H. Chahrour, KDM5A mutations identified in autism spectrum disorder using forward genetics. *eLife* **9**, (2020).
18. E. Brookes, B. Laurent, K. Ounap, R. Carroll, J. B. Moeschler, M. Field, C. E. Schwartz, J. Gecz, Y. Shi, Mutations in the intellectual disability gene KDM5C reduce protein stability and demethylase activity. *Hum Mol Genet* **24**, 2861-2872 (2015).
19. C. N. Vallianatos, C. Farrehi, M. J. Friez, M. Burmeister, C. E. Keegan, S. Iwase, Altered Gene-Regulatory Function of KDM5C by a Novel Mutation Associated With Autism and Intellectual Disability. *Front Mol Neurosci* **11**, 104 (2018).

20. V. Faundes, W. G. Newman, L. Bernardini, N. Canham, J. Clayton-Smith, B. Dallapiccola, S. J. Davies, M. K. Demos, A. Goldman, H. Gill, R. Horton, B. Kerr, D. Kumar, A. Lehman, S. McKee, J. Morton, M. J. Parker, J. Rankin, L. Robertson, I. K. Temple, S. Clinical Assessment of the Utility of, S. Evaluation as a Service, S. Deciphering Developmental Disorders, S. Banka, Histone Lysine Methylases and Demethylases in the Landscape of Human Developmental Disorders. *Am J Hum Genet* **102**, 175-187 (2018).
21. T. Wang, C. N. Kim, T. E. Bakken, M. A. Gillentine, B. Henning, Y. Mao, C. Gilissen, S. Consortium, T. J. Nowakowski, E. E. Eichler, Integrated gene analyses of de novo variants from 46,612 trios with autism and developmental disorders. *Proc Natl Acad Sci U S A* **119**, e2203491119 (2022).
22. T. Wang, P. A. Zhao, E. E. Eichler, Rare variants and the oligogenic architecture of autism. *Trends Genet* **38**, 895-903 (2022).
23. M. Cirnigliaro, T. S. Chang, S. A. Arteaga, L. Perez-Cano, E. K. Ruzzo, A. Gordon, L. K. Bicks, J. Y. Jung, J. K. Lowe, D. P. Wall, D. H. Geschwind, The contributions of rare inherited and polygenic risk to ASD in multiplex families. *Proc Natl Acad Sci U S A* **120**, e2215632120 (2023).
24. H. C. Martin, W. D. Jones, R. McIntyre, G. Sanchez-Andrade, M. Sanderson, J. D. Stephenson, C. P. Jones, J. Handsaker, G. Gallone, M. Bruntraeger, J. F. McRae, E. Prigmore, P. Short, M. Niemi, J. Kaplanis, E. J. Radford, N. Akawi, M. Balasubramanian, J. Dean, R. Horton, A. Hulbert, D. S. Johnson, K. Johnson, D. Kumar, S. A. Lynch, S. G. Mehta, J. Morton, M. J. Parker, M. Splitt, P. D. Turnpenny, P. C. Vasudevan, M. Wright, A. Bassett, S. S. Gerety, C. F. Wright, D. R. FitzPatrick, H. V. Firth, M. E. Hurles, J. C. Barrett, S. Deciphering Developmental Disorders, Quantifying the contribution of recessive coding variation to developmental disorders. *Science* **362**, 1161-1164 (2018).
25. M. C. Borroto, C. Michaud, C. Hudon, P. B. Agrawal, K. Agre, C. D. Applegate, A. H. Beggs, H. T. Bjornsson, B. Callewaert, M. J. Chen, C. Curry, O. Devinsky, T. Dudding-Byth, K. Fagan, C. R. Finnila, R. Gavrilova, C. A. Genetti, S. M. Hiatt, F. Hildebrandt, M. H. Wojcik, T. Kleefstra, C. M. Kolvenbach, B. R. Korf, P. Kruszka, H. Li, J. Litwin, J. Marcadier, K. Platzer, P. R. Blackburn, M. R. F. Reijnders, H. Reutter, I. Schanze, J. T. Shieh, C. A. Stevens, Z. Valivullah, M. J. van den Boogaard, E. W. Klee, P. M. Campeau, A Genotype/Phenotype Study of KDM5B-Associated Disorders Suggests a Pathogenic Effect of Dominantly Inherited Missense Variants. *Genes (Basel)* **15**, (2024).
26. S. Jung, M. Caballero, E. Olfson, J. H. Newcorn, T. V. Fernandez, B. Mahjani, Rare Variant Analyses in Ancestrally Diverse Cohorts Reveal Novel ADHD Risk Genes. *medRxiv*, (2025).
27. E. Olfson, L. C. Farhat, W. Liu, L. A. Vitulano, G. Zai, M. O. Lima, J. Parent, G. V. Polanczyk, C. Cappi, J. L. Kennedy, T. V. Fernandez, Rare de novo damaging DNA variants are enriched in attention-deficit/hyperactivity disorder and implicate risk genes. *Nature communications* **15**, 5870 (2024).
28. M. Albert, S. U. Schmitz, S. M. Kooistra, M. Malatesta, C. Morales Torres, J. C. Rekling, J. V. Johansen, I. Abarrategui, K. Helin, The histone demethylase Jarid1b ensures faithful mouse development by protecting developmental genes from aberrant H3K4me3. *PLoS Genet* **9**, e1003461 (2013).

29. S. Catchpole, B. Spencer-Dene, D. Hall, S. Santangelo, I. Rosewell, M. Guenatri, R. Beatson, A. G. Scibetta, J. M. Burchell, J. Taylor-Papadimitriou, PLU-1/JARID1B/KDM5B is required for embryonic survival and contributes to cell proliferation in the mammary gland and in ER+ breast cancer cells. *Int J Oncol* **38**, 1267-1277 (2011).
30. S. Jamshidi, S. Catchpole, J. Chen, C. W. E. So, J. Burchell, K. M. Rahman, J. Taylor-Papadimitriou, KDM5B protein expressed in viable and fertile DeltaARID mice exhibit no demethylase activity. *Int J Oncol* **59**, (2021).
31. E. J. Lee, S. Y. Choi, E. Kim, NMDA receptor dysfunction in autism spectrum disorders. *Curr Opin Pharmacol* **20**, 8-13 (2015).
32. K. Lee, Z. Mills, P. Cheung, J. E. Cheyne, J. M. Montgomery, The Role of Zinc and NMDA Receptors in Autism Spectrum Disorders. *Pharmaceuticals (Basel)* **16**, (2022).
33. H. Furukawa, S. K. Singh, R. Mancusso, E. Gouaux, Subunit arrangement and function in NMDA receptors. *Nature* **438**, 185-192 (2005).
34. T. Rinaldi, K. Kulangara, K. Antoniello, H. Markram, Elevated NMDA receptor levels and enhanced postsynaptic long-term potentiation induced by prenatal exposure to valproic acid. *Proc Natl Acad Sci U S A* **104**, 13501-13506 (2007).
35. C. Chung, S. Ha, H. Kang, J. Lee, S. M. Um, H. Yan, Y. E. Yoo, T. Yoo, H. Jung, D. Lee, E. Lee, S. Lee, J. Kim, R. Kim, Y. Kwon, W. Kim, H. Kim, L. Duffney, D. Kim, W. Mah, H. Won, S. Mo, J. Y. Kim, C. S. Lim, B. K. Kaang, T. M. Boeckers, Y. Chung, H. Kim, Y. H. Jiang, E. Kim, Early Correction of N-Methyl-D-Aspartate Receptor Function Improves Autistic-like Social Behaviors in Adult Shank2(-/-) Mice. *Biol Psychiatry* **85**, 534-543 (2019).
36. H. Monyer, N. Burnashev, D. J. Laurie, B. Sakmann, P. H. Seeburg, Developmental and regional expression in the rat brain and functional properties of four NMDA receptors. *Neuron* **12**, 529-540 (1994).
37. S. A. Lipton, Paradigm shift in neuroprotection by NMDA receptor blockade: memantine and beyond. *Nat Rev Drug Discov* **5**, 160-170 (2006).
38. W. Chung, S. Y. Choi, E. Lee, H. Park, J. Kang, H. Park, Y. Choi, D. Lee, S. G. Park, R. Kim, Y. S. Cho, J. Choi, M. H. Kim, J. W. Lee, S. Lee, I. Rhim, M. W. Jung, D. Kim, Y. C. Bae, E. Kim, Social deficits in IRSp53 mutant mice improved by NMDAR and mGluR5 suppression. *Nat Neurosci* **18**, 435-443 (2015).
39. J. W. Kim, H. Seung, K. C. Kim, E. L. T. Gonzales, H. A. Oh, S. M. Yang, M. J. Ko, S. H. Han, S. Banerjee, C. Y. Shin, Agmatine rescues autistic behaviors in the valproic acid-induced animal model of autism. *Neuropharmacology* **113**, 71-81 (2017).
40. K. Ma, L. Qin, E. Matas, L. J. Duffney, A. Liu, Z. Yan, Histone deacetylase inhibitor MS-275 restores social and synaptic function in a Shank3-deficient mouse model of autism. *Neuropsychopharmacology* **43**, 1779-1788 (2018).
41. L. Qin, K. Ma, Z. J. Wang, Z. Hu, E. Matas, J. Wei, Z. Yan, Social deficits in Shank3-deficient mouse models of autism are rescued by histone deacetylase (HDAC) inhibition. *Nat Neurosci* **21**, 564-575 (2018).
42. S. Lebon, M. Quinodoz, V. G. Peter, C. Gengler, G. Blanchard, V. Cina, B. Campos-Xavier, C. Rivolta, A. Superti-Furga, Agenesis of the Corpus Callosum with Facial Dysmorphism and Intellectual Disability in Sibs Associated with Compound Heterozygous KDM5B Variants. *Genes (Basel)* **12**, (2021).
43. A. Takata, N. Miyake, Y. Tsurusaki, R. Fukai, S. Miyatake, E. Koshimizu, I. Kushima, T. Okada, M. Morikawa, Y. Uno, K. Ishizuka, K. Nakamura, M. Tsujii, T. Yoshikawa, T.

Toyota, N. Okamoto, Y. Hiraki, R. Hashimoto, Y. Yasuda, S. Saitoh, K. Ohashi, Y. Sakai, S. Ohga, T. Hara, M. Kato, K. Nakamura, A. Ito, C. Seiwa, E. Shirahata, H. Osaka, A. Matsumoto, S. Takeshita, J. Tohyama, T. Saikusa, T. Matsuishi, T. Nakamura, T. Tsuboi, T. Kato, T. Suzuki, H. Saitsu, M. Nakashima, T. Mizuguchi, F. Tanaka, N. Mori, N. Ozaki, N. Matsumoto, Integrative Analyses of De Novo Mutations Provide Deeper Biological Insights into Autism Spectrum Disorder. *Cell Rep* **22**, 734-747 (2018).

44. C. Nava, J. Rupp, J. P. Boissel, C. Mignot, A. Rastetter, C. Amiet, A. Jacquette, C. Dupuits, D. Bouteiller, B. Keren, M. Ruberg, A. Faudet, D. Doummar, A. Philippe, D. Perisse, C. Laurent, N. Lebrun, V. Guillemot, J. Chelly, D. Cohen, D. Heron, A. Brice, E. I. Closs, C. Depienne, Hypomorphic variants of cationic amino acid transporter 3 in males with autism spectrum disorders. *Amino Acids* **47**, 2647-2658 (2015).
45. E. Perez-Palma, E. Saarentaus, M. Ravoet, G. V. De Ferrari, P. Nurnberg, B. Isidor, B. A. Neubauer, D. Lal, Duplications at 19q13.33 in patients with neurodevelopmental disorders. *Neurol Genet* **4**, e210 (2018).
46. D. Li, H. Yuan, X. R. Ortiz-Gonzalez, E. D. Marsh, L. Tian, E. M. McCormick, G. J. Kosobucki, W. Chen, A. J. Schulien, R. Chiavacci, A. Tankovic, C. Naase, F. Brueckner, C. von Stulpnagel-Steinbeis, C. Hu, H. Kusumoto, U. B. Hedrich, G. Elsen, K. Hortnagel, E. Aizenman, J. R. Lemke, H. Hakonarson, S. F. Traynelis, M. J. Falk, GRIN2D Recurrent De Novo Dominant Mutation Causes a Severe Epileptic Encephalopathy Treatable with NMDA Receptor Channel Blockers. *Am J Hum Genet* **99**, 802-816 (2016).
47. W. XiangWei, V. Kannan, Y. Xu, G. J. Kosobucki, A. J. Schulien, H. Kusumoto, C. Moufawad El Achkar, S. Bhattacharya, G. Lesca, S. Nguyen, K. L. Helbig, J. M. Cuisset, C. D. Fenger, D. Marjanovic, E. Schuler, Y. Wu, X. Bao, Y. Zhang, N. Dirkx, A. S. Schoonjans, S. Syrbe, S. J. Myers, A. Poduri, E. Aizenman, S. F. Traynelis, J. R. Lemke, H. Yuan, Y. Jiang, Heterogeneous clinical and functional features of GRIN2D-related developmental and epileptic encephalopathy. *Brain : a journal of neurology* **142**, 3009-3027 (2019).
48. A. E. Jaffe, R. E. Straub, J. H. Shin, R. Tao, Y. Gao, L. Collado-Torres, T. Kam-Thong, H. S. Xi, J. Quan, Q. Chen, C. Colantuoni, W. S. Ulrich, B. J. Maher, A. Deep-Soboslay, C. BrainSeq, A. J. Cross, N. J. Brandon, J. T. Leek, T. M. Hyde, J. E. Kleinman, D. R. Weinberger, Developmental and genetic regulation of the human cortex transcriptome illuminate schizophrenia pathogenesis. *Nat Neurosci* **21**, 1117-1125 (2018).
49. N. E. Clifton, M. L. Bosworth, N. Haan, E. Rees, P. A. Holmans, L. S. Wilkinson, A. R. Isles, M. O. Collins, J. Hall, Developmental disruption to the cortical transcriptome and synaptosome in a model of SETD1A loss-of-function. *Hum Mol Genet* **31**, 3095-3106 (2022).
50. J. F. Zander, A. Munster-Wandowski, I. Brunk, I. Pahner, G. Gomez-Lira, U. Heinemann, R. Gutierrez, G. Laube, G. Ahnert-Hilger, Synaptic and vesicular coexistence of VGLUT and VGAT in selected excitatory and inhibitory synapses. *J Neurosci* **30**, 7634-7645 (2010).
51. G. M. Durand, Y. Kovalchuk, A. Konnerth, Long-term potentiation and functional synapse induction in developing hippocampus. *Nature* **381**, 71-75 (1996).
52. S. Rumpel, H. Hatt, K. Gottmann, Silent synapses in the developing rat visual cortex: evidence for postsynaptic expression of synaptic plasticity. *J Neurosci* **18**, 8863-8874 (1998).

53. T. M. Pierson, H. Yuan, E. D. Marsh, K. Fuentes-Fajardo, D. R. Adams, T. Markello, G. Golas, D. R. Simeonov, C. Holloman, A. Tankovic, M. M. Karamchandani, J. M. Schreiber, J. C. Mullikin, D. f. t. N. C. S. P. Ph, C. J. Tifft, C. Toro, C. F. Boerkoel, S. F. Traynelis, W. A. Gahl, GRIN2A mutation and early-onset epileptic encephalopathy: personalized therapy with memantine. *Ann Clin Transl Neurol* **1**, 190-198 (2014).
54. M. G. Beconi, D. Howland, L. Park, K. Lyons, J. Giuliano, C. Dominguez, I. Munoz-Sanjuan, R. Pacifici, Pharmacokinetics of memantine in rats and mice. *PLoS Curr* **3**, RRN1291 (2011).
55. N. Egashira, R. Okuno, S. Harada, M. Matsushita, K. Mishima, K. Iwasaki, R. Nishimura, R. Oishi, M. Fujiwara, Effects of glutamate-related drugs on marble-burying behavior in mice: implications for obsessive-compulsive disorder. *Eur J Pharmacol* **586**, 164-170 (2008).
56. J. Kang, E. Kim, Suppression of NMDA receptor function in mice prenatally exposed to valproic acid improves social deficits and repetitive behaviors. *Front Mol Neurosci* **8**, 17 (2015).
57. S. Tang, B. Terzic, I. J. Wang, N. Sarmiento, K. Sizov, Y. Cui, H. Takano, E. D. Marsh, Z. Zhou, D. A. Coulter, Altered NMDAR signaling underlies autistic-like features in mouse models of CDKL5 deficiency disorder. *Nature communications* **10**, 2655 (2019).
58. C. P. Figueiredo, J. R. Clarke, J. H. Ledo, F. C. Ribeiro, C. V. Costa, H. M. Melo, A. P. Mota-Sales, L. M. Saraiva, W. L. Klein, A. Sebollela, F. G. De Felice, S. T. Ferreira, Memantine rescues transient cognitive impairment caused by high-molecular-weight abeta oligomers but not the persistent impairment induced by low-molecular-weight oligomers. *J Neurosci* **33**, 9626-9634 (2013).
59. S. De Rubeis, X. He, A. P. Goldberg, C. S. Poultney, K. Samocha, A. E. Cicek, Y. Kou, L. Liu, M. Fromer, S. Walker, T. Singh, L. Klei, J. Kosmicki, F. Shih-Chen, B. Aleksic, M. Biscaldi, P. F. Bolton, J. M. Brownfeld, J. Cai, N. G. Campbell, A. Carracedo, M. H. Chahrour, A. G. Chiocchetti, H. Coon, E. L. Crawford, S. R. Curran, G. Dawson, E. Duketis, B. A. Fernandez, L. Gallagher, E. Geller, S. J. Guter, R. S. Hill, J. Ionita-Laza, P. Jimenz Gonzalez, H. Kilpinen, S. M. Klauck, A. Kolevzon, I. Lee, I. Lei, J. Lei, T. Lehtimaki, C. F. Lin, A. Ma'ayan, C. R. Marshall, A. L. McInnes, B. Neale, M. J. Owen, N. Ozaki, M. Parellada, J. R. Parr, S. Purcell, K. Puura, D. Rajagopalan, K. Rehnstrom, A. Reichenberg, A. Sabo, M. Sachse, S. J. Sanders, C. Schafer, M. Schulte-Ruther, D. Skuse, C. Stevens, P. Szatmari, K. Tammimies, O. Valladares, A. Voran, W. Li-San, L. A. Weiss, A. J. Willsey, T. W. Yu, R. K. Yuen, D. D. D. Study, A. Homozygosity Mapping Collaborative for, U. K. Consortium, E. H. Cook, C. M. Freitag, M. Gill, C. M. Hultman, T. Lehner, A. Palotie, G. D. Schellenberg, P. Sklar, M. W. State, J. S. Sutcliffe, C. A. Walsh, S. W. Scherer, M. E. Zwick, J. C. Barett, D. J. Cutler, K. Roeder, B. Devlin, M. J. Daly, J. D. Buxbaum, Synaptic, transcriptional and chromatin genes disrupted in autism. *Nature* **515**, 209-215 (2014).
60. J. Homsy, S. Zaidi, Y. Shen, J. S. Ware, K. E. Samocha, K. J. Karczewski, S. R. DePalma, D. McKean, H. Wakimoto, J. Gorham, S. C. Jin, J. Deanfield, A. Giardini, G. A. Porter, Jr., R. Kim, K. Bilguvar, F. Lopez-Giraldez, I. Tikhonova, S. Mane, A. Romano-Adesman, H. Qi, B. Vardarajan, L. Ma, M. Daly, A. E. Roberts, M. W. Russell, S. Mital, J. W. Newburger, J. W. Gaynor, R. E. Breitbart, I. Iossifov, M. Ronemus, S. J. Sanders, J. R. Kaltman, J. G. Seidman, M. Brueckner, B. D. Gelb, E. Goldmuntz, R. P. Lifton, C. E. Seidman, W. K. Chung, De novo mutations in congenital heart disease with

neurodevelopmental and other congenital anomalies. *Science* **350**, 1262-1266 (2015).
61. T. V. Fernandez, Z. P. Williams, T. Kline, S. Rajendran, F. Augustine, N. Wright, C. A. W. Sullivan, E. Olfson, S. B. Abdallah, W. Liu, E. J. Hoffman, A. R. Gupta, H. S. Singer, Primary complex motor stereotypies are associated with de novo damaging DNA coding mutations that identify KDM5B as a risk gene. *PLoS One* **18**, e0291978 (2023).
62. K. Tan, A. L. Shaw, B. Madsen, K. Jensen, J. Taylor-Papadimitriou, P. S. Freemont, Human PLU-1 Has transcriptional repression properties and interacts with the developmental transcription factors BF-1 and PAX9. *J Biol Chem* **278**, 20507-20513 (2003).
63. A. Barrett, S. Santangelo, K. Tan, S. Catchpole, K. Roberts, B. Spencer-Dene, D. Hall, A. Scibetta, J. Burchell, E. Verdin, P. Freemont, J. Taylor-Papadimitriou, Breast cancer associated transcriptional repressor PLU-1/JARID1B interacts directly with histone deacetylases. *Int J Cancer* **121**, 265-275 (2007).
64. M. T. Dang, F. Yokoi, H. H. Yin, D. M. Lovinger, Y. Wang, Y. Li, Disrupted motor learning and long-term synaptic plasticity in mice lacking NMDAR1 in the striatum. *Proc Natl Acad Sci U S A* **103**, 15254-15259 (2006).
65. S. L. Dean, L. Tochen, F. Augustine, S. F. Ali, D. Crocetti, S. Rajendran, M. E. Blue, E. M. Mahone, S. H. Mostofsky, H. S. Singer, The Role of the Cerebellum in Repetitive Behavior Across Species: Childhood Stereotypies and Deer Mice. *Cerebellum* **21**, 440-451 (2022).
66. J. C. Carter, G. T. Capone, W. E. Kaufmann, Neuroanatomic correlates of autism and stereotypy in children with Down syndrome. *Neuroreport* **19**, 653-656 (2008).
67. A. E. Kelley, C. G. Lang, A. M. Gauthier, Induction of oral stereotypy following amphetamine microinjection into a discrete subregion of the striatum. *Psychopharmacology* **95**, 556-559 (1988).
68. S. Sato, T. Hashimoto, A. Nakamura, S. Ikeda, Stereotyped stepping associated with lesions in the bilateral medial frontoparietal cortices. *Neurology* **57**, 711-713 (2001).
69. P. Suetterlin, S. Hurley, C. Mohan, K. L. H. Riegman, M. Pagani, A. Caruso, J. Ellegood, A. Galbusera, I. Crespo-Enriquez, C. Michetti, Y. Yee, R. Ellingford, O. Brock, A. Delogu, P. Francis-West, J. P. Lerch, M. L. Scattoni, A. Gozzi, C. Fernandes, M. A. Basson, Altered Neocortical Gene Expression, Brain Overgrowth and Functional Over-Connectivity in Chd8 Haploinsufficient Mice. *Cereb Cortex* **28**, 2192-2206 (2018).
70. A. L. Gompers, L. Su-Feher, J. Ellegood, N. A. Copping, M. A. Riyadh, T. W. Stradleigh, M. C. Pride, M. D. Schaffler, A. A. Wade, R. Catta-Preta, I. Zdilar, S. Louis, G. Kaushik, B. J. Mannion, I. Plajzer-Frick, V. Afzal, A. Visel, L. A. Pennacchio, D. E. Dickel, J. P. Lerch, J. N. Crawley, K. S. Zarbalis, J. L. Silverman, A. S. Nord, Germline Chd8 haploinsufficiency alters brain development in mouse. *Nat Neurosci* **20**, 1062-1073 (2017).
71. S. Hurley, C. Mohan, P. Suetterlin, R. Ellingford, K. L. H. Riegman, J. Ellegood, A. Caruso, C. Michetti, O. Brock, R. Evans, F. Rudari, A. Delogu, M. L. Scattoni, J. P. Lerch, C. Fernandes, M. A. Basson, Distinct, dosage-sensitive requirements for the autism-associated factor CHD8 during cortical development. *Mol Autism* **12**, 16 (2021).
72. H. Jung, H. Park, Y. Choi, H. Kang, E. Lee, H. Kweon, J. D. Roh, J. Ellegood, W. Choi, J. Kang, I. Rhim, S. Y. Choi, M. Bae, S. G. Kim, J. Lee, C. Chung, T. Yoo, H. Park, Y. Kim, S.

Ha, S. M. Um, S. Mo, Y. Kwon, W. Mah, Y. C. Bae, H. Kim, J. P. Lerch, S. B. Paik, E. Kim, Sexually dimorphic behavior, neuronal activity, and gene expression in Chd8-mutant mice. *Nat Neurosci* **21**, 1218-1228 (2018).

73. Y. Katayama, M. Nishiyama, H. Shoji, Y. Ohkawa, A. Kawamura, T. Sato, M. Suyama, T. Takumi, T. Miyakawa, K. I. Nakayama, CHD8 haploinsufficiency results in autistic-like phenotypes in mice. *Nature* **537**, 675-679 (2016).
74. R. J. Platt, Y. Zhou, I. M. Slaymaker, A. S. Shetty, N. R. Weisbach, J. A. Kim, J. Sharma, M. Desai, S. Sood, H. R. Kempton, G. R. Crabtree, G. Feng, F. Zhang, Chd8 Mutation Leads to Autistic-like Behaviors and Impaired Striatal Circuits. *Cell Rep* **19**, 335-350 (2017).
75. X. Song, M. O. Jensen, V. Jogini, R. A. Stein, C. H. Lee, H. S. McHaourab, D. E. Shaw, E. Gouaux, Mechanism of NMDA receptor channel block by MK-801 and memantine. *Nature* **556**, 515-519 (2018).
76. C. Akazawa, R. Shigemoto, Y. Bessho, S. Nakanishi, N. Mizuno, Differential expression of five N-methyl-D-aspartate receptor subunit mRNAs in the cerebellum of developing and adult rats. *J Comp Neurol* **347**, 150-160 (1994).
77. R. E. Perszyk, J. O. DiRaddo, K. L. Strong, C. M. Low, K. K. Ogden, A. Khatri, G. A. Vargish, K. A. Pelkey, L. Tricoire, D. C. Liotta, Y. Smith, C. J. McBain, S. F. Traynelis, GluN2D-Containing N-methyl-d-Aspartate Receptors Mediate Synaptic Transmission in Hippocampal Interneurons and Regulate Interneuron Activity. *Mol Pharmacol* **90**, 689-702 (2016).
78. A. V. Eapen, D. Fernandez-Fernandez, J. Georgiou, Z. A. Bortolotto, S. Lightman, D. E. Jane, A. Volianskis, G. L. Collingridge, Multiple roles of GluN2D-containing NMDA receptors in short-term potentiation and long-term potentiation in mouse hippocampal slices. *Neuropharmacology* **201**, 108833 (2021).
79. N. Tsuchida, K. Hamada, M. Shiina, M. Kato, Y. Kobayashi, J. Tohyama, K. Kimura, K. Hoshino, V. Ganesan, K. W. Teik, M. Nakashima, S. Mitsuhashi, T. Mizuguchi, A. Takata, N. Miyake, H. Saitsu, K. Ogata, S. Miyatake, N. Matsumoto, GRIN2D variants in three cases of developmental and epileptic encephalopathy. *Clin Genet* **94**, 538-547 (2018).
80. A. M. Bertoli-Avella, C. Beetz, N. Ameziane, M. E. Rocha, P. Guatibonza, C. Pereira, M. Calvo, N. Herrera-Ordonez, M. Segura-Castel, D. Diego-Alvarez, M. Zawada, K. K. Kandaswamy, M. Werber, O. Paknia, S. Zielske, D. Ugrinovski, G. Warnack, K. Kampe, M. I. Iurascu, C. Cozma, F. Vogel, A. Alhashem, J. Hertecant, A. M. Al-Shamsi, A. F. Alswaid, W. Eyaid, F. Al Mutairi, A. Alfares, M. A. Albalwi, M. Alfadhel, N. A. Al-Sannaa, W. Reardon, Y. Alanay, A. Rolfs, P. Bauer, Successful application of genome sequencing in a diagnostic setting: 1007 index cases from a clinically heterogeneous cohort. *Eur J Hum Genet* **29**, 141-153 (2021).
81. J. Jiao, L. Li, M. Sun, J. Fang, L. Meng, Y. Zhang, C. Jia, L. Ma, Identification of a novel GRIN2D variant in a neonate with intractable epileptic encephalopathy-a case report. *BMC Pediatr* **21**, 5 (2021).
82. G. D. Mangano, V. Antona, E. Cali, A. Fontana, V. Salpietro, H. Houlden, P. Veggiotti, R. Nardello, A complex epileptic and dysmorphic phenotype associated with a novel frameshift KDM5B variant and deletion of SCN gene cluster. *Seizure* **97**, 20-22 (2022).
83. M. Karahmadi, M. J. Tarrahi, S. S. Vatankhah Ardestani, V. Omranifard, B. Farzaneh, Efficacy of Memantine as Adjunct Therapy for Autism Spectrum Disorder in Children Aged <14 Years. *Adv Biomed Res* **7**, 131 (2018).

84. A. Brignell, C. Marraffa, K. Williams, T. May, Memantine for autism spectrum disorder. *Cochrane Database Syst Rev* **8**, CD013845 (2022).
85. G. Joshi, J. Wozniak, S. V. Faraone, R. Fried, J. Chan, S. Furtak, E. Grimsley, K. Conroy, J. R. Kilcullen, K. Y. Woodworth, J. Biederman, A Prospective Open-Label Trial of Memantine Hydrochloride for the Treatment of Social Deficits in Intellectually Capable Adults With Autism Spectrum Disorder. *J Clin Psychopharmacol* **36**, 262-271 (2016).
86. L. V. Soorya, L. Fogg, E. Ocampo, M. Printen, S. Youngkin, D. Halpern, A. Kolevzon, S. Lee, D. Grodberg, E. Anagnostou, Neurocognitive Outcomes from Memantine: A Pilot, Double-Blind, Placebo-Controlled Trial in Children with Autism Spectrum Disorder. *J Child Adolesc Psychopharmacol* **31**, 475-484 (2021).
87. S. Bouhadoun, C. Poulin, S. Berrahmoune, K. A. Myers, A retrospective analysis of memantine use in a pediatric neurology clinic. *Brain Dev* **43**, 997-1003 (2021).
88. D. J. Smits, R. Schot, C. A. Popescu, K. R. Dias, L. Ades, L. C. Briere, D. A. Sweetser, I. Kushima, B. Aleksic, S. Khan, V. Karageorgou, N. Ordonez, F. Sleutels, D. C. M. van der Kaay, C. Van Mol, H. Van Esch, A. M. Bertoli-Avella, T. Roscioli, G. M. S. Mancini, De novo MCM6 variants in neurodevelopmental disorders: a recognizable phenotype related to zinc binding residues. *Hum Genet* **142**, 949-964 (2023).
89. A. Stuermer, K. Hoehn, T. Faul, T. Auth, N. Brand, M. Kneissl, V. Putter, F. Grummt, Mouse pre-replicative complex proteins colocalise and interact with the centrosome. *Eur J Cell Biol* **86**, 37-50 (2007).
90. Q. Zhou, E. A. Obana, K. L. Radomski, G. Sukumar, C. Wynder, C. L. Dalgard, M. L. Doughty, Inhibition of the histone demethylase Kdm5b promotes neurogenesis and derepresses Reln (reelin) in neural stem cells from the adult subventricular zone of mice. *Mol Biol Cell* **27**, 627-639 (2016).
91. G. E. Truett, P. Heeger, R. L. Mynatt, A. A. Truett, J. A. Walker, M. L. Warman, Preparation of PCR-quality mouse genomic DNA with hot sodium hydroxide and tris (HotSHOT). *Biotechniques* **29**, 52, 54 (2000).
92. E. Romano, C. Michetti, A. Caruso, G. Laviola, M. L. Scattoni, Characterization of neonatal vocal and motor repertoire of reelin mutant mice. *PLoS One* **8**, e64407 (2013).
93. A. Takahashi, J. J. Yap, D. Z. Bohager, S. Faccidomo, T. Clayton, J. M. Cook, K. A. Miczek, Glutamatergic and GABAergic modulations of ultrasonic vocalizations during maternal separation distress in mouse pups. *Psychopharmacology* **204**, 61-71 (2009).
94. J. P. Lerch, J. G. Sled, R. M. Henkelman, MRI phenotyping of genetically altered mice. *Methods Mol Biol* **711**, 349-361 (2011).
95. A. E. de Guzman, M. D. Wong, J. A. Gleave, B. J. Nieman, Variations in post-perfusion immersion fixation and storage alter MRI measurements of mouse brain morphometry. *NeuroImage* **142**, 687-695 (2016).
96. B. B. Avants, C. L. Epstein, M. Grossman, J. C. Gee, Symmetric diffeomorphic image registration with cross-correlation: evaluating automated labeling of elderly and neurodegenerative brain. *Med Image Anal* **12**, 26-41 (2008).
97. B. J. Nieman, A. M. Flenniken, S. L. Adamson, R. M. Henkelman, J. G. Sled, Anatomical phenotyping in the brain and skull of a mutant mouse by magnetic resonance imaging and computed tomography. *Physiol Genomics* **24**, 154-162 (2006).

98. J. P. Lerch, J. B. Carroll, S. Spring, L. N. Bertram, C. Schwab, M. R. Hayden, R. M. Henkelman, Automated deformation analysis in the YAC128 Huntington disease mouse model. *NeuroImage* **39**, 32-39 (2008).
99. A. E. Dorr, J. P. Lerch, S. Spring, N. Kabani, R. M. Henkelman, High resolution three-dimensional brain atlas using an average magnetic resonance image of 40 adult C57Bl/6J mice. *NeuroImage* **42**, 60-69 (2008).
100. L. R. Qiu, D. J. Fernandes, K. U. Szulc-Lerch, J. Dazai, B. J. Nieman, D. H. Turnbull, J. A. Foster, M. R. Palmert, J. P. Lerch, Mouse MRI shows brain areas relatively larger in males emerge before those larger in females. *Nature communications* **9**, 2615 (2018).
101. K. Richards, C. Watson, R. F. Buckley, N. D. Kurniawan, Z. Yang, M. D. Keller, R. Beare, P. F. Bartlett, G. F. Egan, G. J. Galloway, G. Paxinos, S. Petrou, D. C. Reutens, Segmentation of the mouse hippocampal formation in magnetic resonance images. *NeuroImage* **58**, 732-740 (2011).
102. P. E. Steadman, J. Ellegood, K. U. Szulc, D. H. Turnbull, A. L. Joyner, R. M. Henkelman, J. P. Lerch, Genetic effects on cerebellar structure across mouse models of autism using a magnetic resonance imaging atlas. *Autism research : official journal of the International Society for Autism Research* **7**, 124-137 (2014).
103. J. F. Ullmann, C. Watson, A. L. Janke, N. D. Kurniawan, D. C. Reutens, A segmentation protocol and MRI atlas of the C57BL/6J mouse neocortex. *NeuroImage* **78**, 196-203 (2013).
104. C. R. Genovese, N. A. Lazar, T. Nichols, Thresholding of statistical maps in functional neuroimaging using the false discovery rate. *NeuroImage* **15**, 870-878 (2002).
105. U. Raudvere, L. Kolberg, I. Kuzmin, T. Arak, P. Adler, H. Peterson, J. Vilo, g:Profiler: a web server for functional enrichment analysis and conversions of gene lists (2019 update). *Nucleic Acids Res* **47**, W191-W198 (2019).
106. P. A. Ewels, A. Peltzer, S. Fillinger, H. Patel, J. Alneberg, A. Wilm, M. U. Garcia, P. Di Tommaso, S. Nahnsen, The nf-core framework for community-curated bioinformatics pipelines. *Nat Biotechnol* **38**, 276-278 (2020).
107. P. Di Tommaso, M. Chatzou, E. W. Floden, P. P. Barja, E. Palumbo, C. Notredame, Nextflow enables reproducible computational workflows. *Nat Biotechnol* **35**, 316-319 (2017).
108. B. Langmead, S. L. Salzberg, Fast gapped-read alignment with Bowtie 2. *Nat Methods* **9**, 357-359 (2012).
109. P. Danecek, J. K. Bonfield, J. Liddle, J. Marshall, V. Ohan, M. O. Pollard, A. Whitwham, T. Keane, S. A. McCarthy, R. M. Davies, H. Li, Twelve years of SAMtools and BCFtools. *Gigascience* **10**, (2021).
110. M. P. Meers, D. Tenenbaum, S. Henikoff, Peak calling by Sparse Enrichment Analysis for CUT&RUN chromatin profiling. *Epigenetics Chromatin* **12**, 42 (2019).
111. F. Ramirez, D. P. Ryan, B. Gruning, V. Bhardwaj, F. Kilpert, A. S. Richter, S. Heyne, F. Dundar, T. Manke, deepTools2: a next generation web server for deep-sequencing data analysis. *Nucleic Acids Res* **44**, W160-165 (2016).
112. M. D. Luecken, F. J. Theis, Current best practices in single-cell RNA-seq analysis: a tutorial. *Mol Syst Biol* **15**, e8746 (2019).
113. A. T. Lun, D. J. McCarthy, J. C. Marioni, A step-by-step workflow for low-level analysis of single-cell RNA-seq data with Bioconductor. *F1000Res* **5**, 2122 (2016).

114. D. J. Di Bella, E. Habibi, R. R. Stickels, G. Scalia, J. Brown, P. Yadollahpour, S. M. Yang, C. Abbate, T. Biancalani, E. Z. Macosko, F. Chen, A. Regev, P. Arlotta, Molecular logic of cellular diversification in the mouse cerebral cortex. *Nature* **595**, 554-559 (2021).
115. Z. Yao, C. T. J. van Velthoven, T. N. Nguyen, J. Goldy, A. E. Sedeno-Cortes, F. Baftizadeh, D. Bertagnolli, T. Casper, M. Chiang, K. Crichton, S. L. Ding, O. Fong, E. Garren, A. Glandon, N. W. Gouwens, J. Gray, L. T. Graybuck, M. J. Hawrylycz, D. Hirschstein, M. Kroll, K. Lathia, C. Lee, B. Levi, D. McMillen, S. Mok, T. Pham, Q. Ren, C. Rimorin, N. Shapovalova, J. Sulc, S. M. Sunkin, M. Tieu, A. Torkelson, H. Tung, K. Ward, N. Dee, K. A. Smith, B. Tasic, H. Zeng, A taxonomy of transcriptomic cell types across the isocortex and hippocampal formation. *Cell* **184**, 3222-3241 e3226 (2021).

Acknowledgements

We thank animal husbandry staff at KCL for expert animal care. We thank our laboratory colleagues for comments on the manuscript. The Galaxy server that was used for some of the analysis is in part funded by Collaborative Research Centre 992 Medical Epigenetics (DFG grant SFB 992/1 2012) and German Federal Ministry of Education and Research (BMBF grants 031 A538A/A538C RBC, 031L0101B/031L0101C de.NBI-epi, 031L0106 de.STAIR (de.NBI)).

Funding

This work was supported by Medical Research Council grants MR/V013173/1 (MAB and KPG), MR/Y008170/1 (MAB), MR/X010481/1 (LCA and MAB) and MR/W017156/1 (NEC).

Author contributions

MAB and LPS conceived the study and designed the experiments. LPS, SB, AC, JLR, RB, MP, JT, NJ, TG, SS, EH,JE and MAB performed the experiments and analysed the data. LPS, APAD, ATC and MA performed bioinformatic analyses. JTP provided the *Kdm5b*-deficient mouse line and associated expertise. DC provided advice and assistance with memantine experiments. NC, LCA, JL, MLS, KPG, CF and MAB oversaw the research and analysis. LPS and MAB wrote the manuscript with input from co-authors.

Competing interests

The authors have declared that no conflict of interest exists.

Data and material availability

All data needed to evaluate the conclusions in the paper are available in the main text and/or the supplementary materials. RNA-seq, CUT&Tag-seq and Parse snRNA-seq raw data has been deposited at the Gene Expression Omnibus (GEO) archive (GSE262555) and will be made freely available upon publication. The snRNA-seq analysis code will be released on Zenodo (https://doi.org/10.5281/zenodo.17466762) once the manuscript is accepted for publication. The *Kdm5b* mouse line can be provided by JTP pending scientific review and a completed material transfer agreement. Requests for the mouse line should be submitted to: joyce.taylor-papadimitriou@kcl.ac.uk.

FIGURES

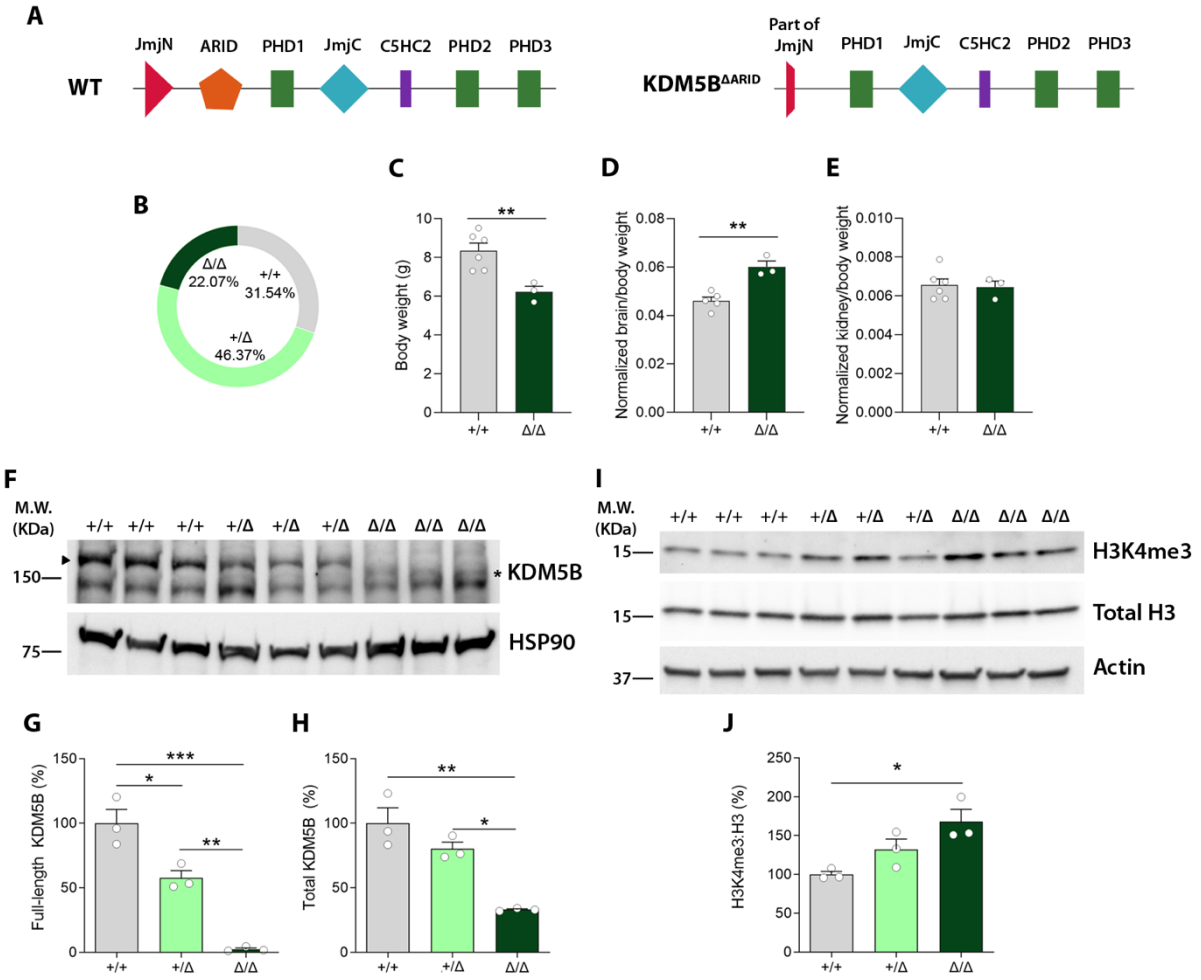

Fig. 1. Developmental alterations and KDM5B expression in control and ΔARID mice. A) Schematic representations of mouse KDM5B WT and ΔARID protein domains. Note that transgenic *Kdm5b ΔARID* mice carry a deletion of the entire ARID domain and a truncation of the carboxyl end of the JmjN domain. **B)** Genotyping frequencies show no statistically significant differences between genotypes (Chi-square test) at postnatal day (PND) 21. **C-E)** *Kdm5b ΔARID* homozygous mice (*Kdm5b*$^{\Delta/\Delta}$) exhibit decreased weight and increased brain-to-body weight ratios with no difference in kidney-to-body weight ratios.. N= 5-6 +/+ and 3 Δ/Δ mice. **F-H)** Estimation of full-length (G) and total (H; full length and truncated) KDM5B protein expression by western blot in neocortical samples extracted from P5 animals. HSP90 was used as loading control. Arrowhead: Full-length KDM5B isoform; asterisk: truncated ΔARID protein. **I,J)** H3K4me3 and total H3 levels in WT, heterozygous and ΔARID homozygous mice in neocortical samples extracted from PND5 animals. Wild type (+/+) and ΔARID heterozygous (+/Δ) and homozygous (Δ/Δ) mice. Data is shown

as percentage versus WT average. N= 3 +/+ and 3 Δ/Δ mice. Data is shown as mean ±SEM and was analysed with One-way ANOVA followed by Tukey's multiple comparisons test. *p<0.05, **p<0.01 and ***p<0.001.

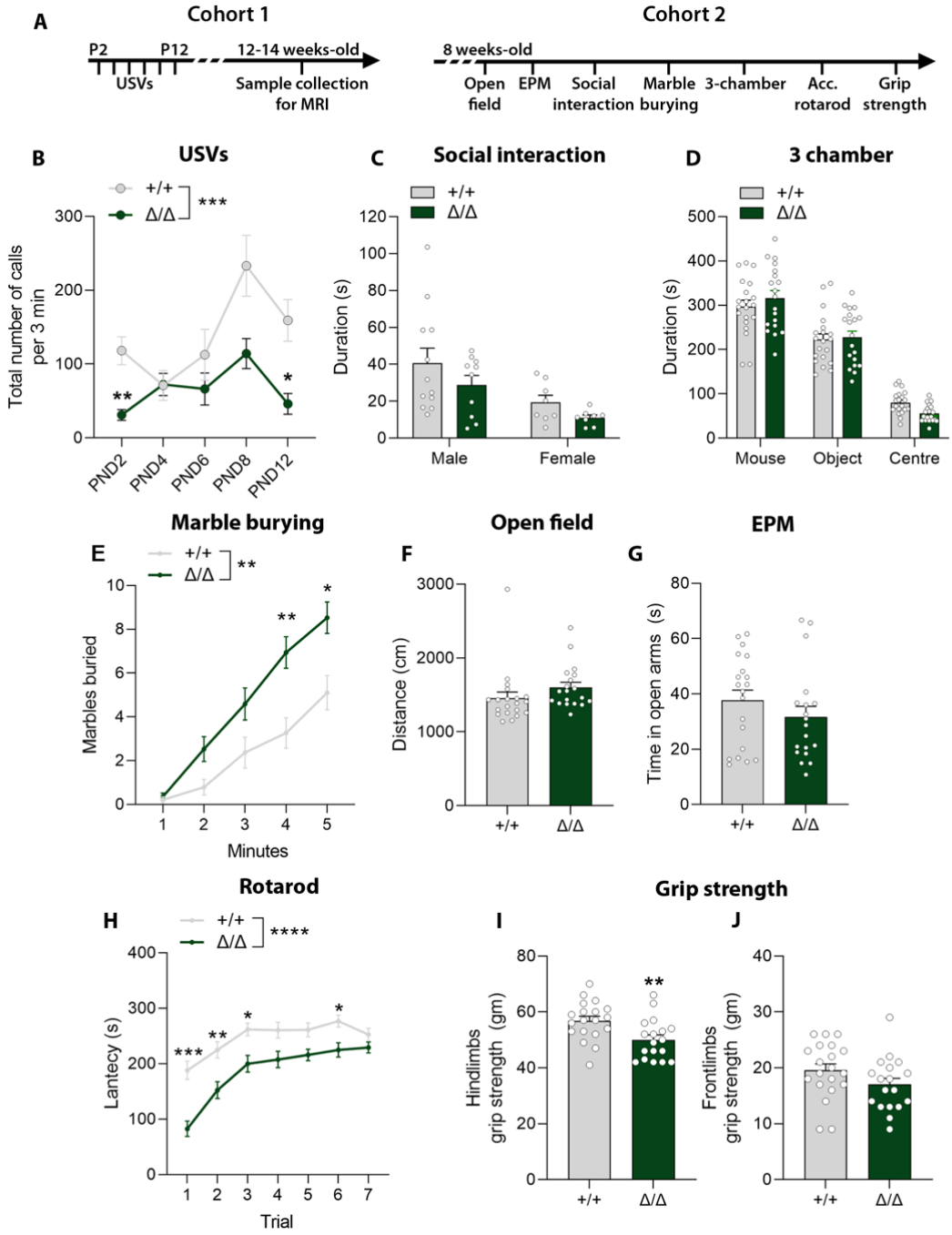

Fig. 2. Behavioural assessment of *Kdm5b*$^{\Delta/\Delta}$ mice. Behavioural assessment of a cohort of neonatal (B) (+/+ N=3 males and 7 females; Δ/Δ N=6 males and 6 females) and adult mice (C-J) (+/+ n=11-12 males and 7-8 females; Δ/Δ n=10-11 males and 6-8 females). **A)** Experimental time-course. Note that different cohorts were used for

experiments with neonatal and adult mice. **B)** Total number of ultrasonic vocalizations (USVs) during 3 minutes testing sessions on indicated postnatal days. Repeated measures two-way ANOVA Interaction: $F_{(4,80)}$=2.866, *p=0.0284; Genotype effect: $F_{(1,20)}$=15.03, ***p=0.0009. **C)** Duration, in seconds, of social investigation, defined as total duration of sniffing above the shoulders of a conspecific mouse. Two-way ANOVA sex effect: $F_{(1,34)}$=9.785, **p=0.0036. **D)** Time spent, in seconds, in each chamber in the 3 chamber sociability test. **E)** Number of marbles buried during a 5 minute test. Repeated measures two-way ANOVA Interaction: $F_{(4, 136)}$=5.894, ****p=0.0002; Genotype effect: $F_{(1,34)}$=11.08, **p=0.0021. **F)** Distance traveled in the outer area of an open field arena during a 5 minute test. **G)** Time spent in the open arms of the elevated plus maze (EPM) is shown. **H)** Mean latency of mice to fall from the rotarod during 7 trials in one day. Repeated measures two-way ANOVA Interaction: $F_{(6,222)}$=2.944, **p=0.0088; Genotype effect: $F_{(1,37)}$=21.54, ****p<0.0001. **I,J)** Hind- and frontlimb grip strength measurements. Data is shown as mean ±SEM and was analysed with Two-way ANOVA (C,D), repeated measures ANOVA (B,E,H) followed by Sidak's post hoc test, and Student's t-test (F,G,I,J). *P<0.05, **P<0.01 and ***P<0.001.

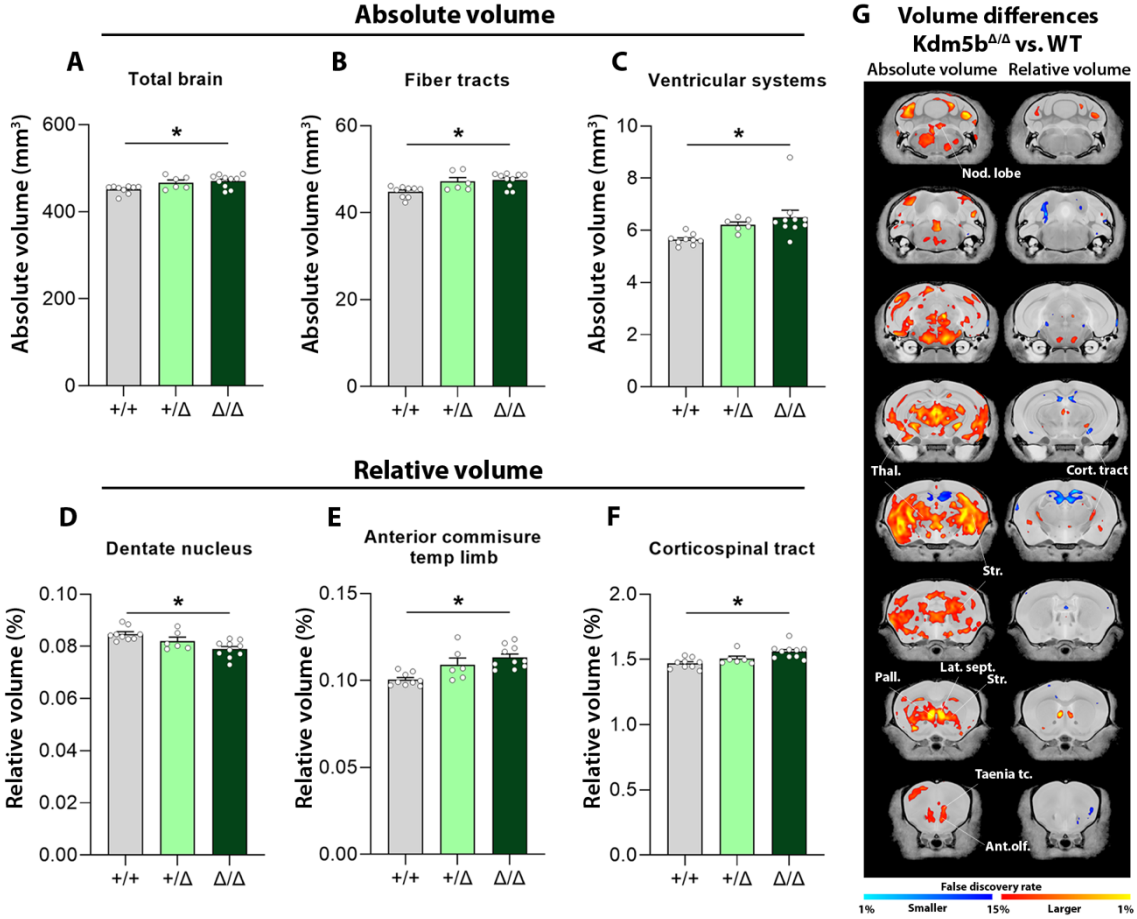

Fig. 3. *Kdm5b*$^{\Delta/\Delta}$ mutant mice display megalencephaly and altered regional volume of different brain areas. A-C) MRI analysis revealed significant increases in absolute brain size together with increased regional volume of different brain areas such as the fiber tracts and the ventricular systems. **D-F)** Correction for absolute brain volume revealed significant changes in volume in the dentate nucleus, corticospinal tract and anterior commissure of the temporal limb. **G)** Voxel-wise differences in volume (absolute, left; relative, right) between wild-type and *Kdm5b*$^{\Delta/\Delta}$ mutant littermates. Data is shown as mean ±SEM. Multiple comparisons (all brain regions) were controlled for using the False Discovery Rate (see Tables S1-4). *FDR<0.05. N= 9 +/+, 5 +/Δ and 10 Δ/Δ animals. Nod. lobe, cerebellar nodular lobe; Thal., thalamus; Cort. tract, corticospinal tract; Str., striatum; Pall., pallidum; Lat. Sep., lateral septum; Taenia tc., taenia tecta; Ant. olf., anterior olfactory nucleus.

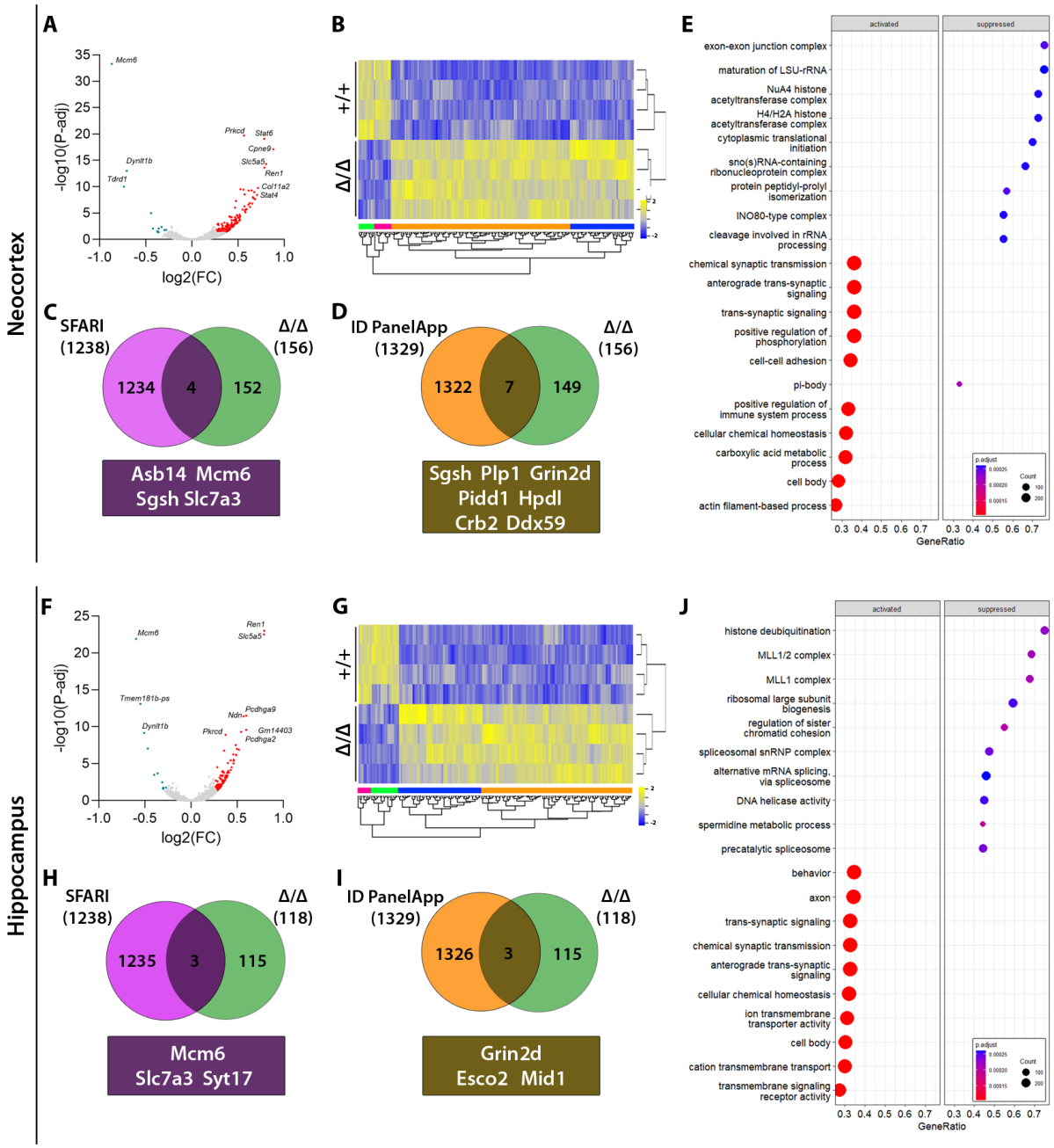

Fig. 4. Gene expression changes in PND5 *Kdm5b*$^{\Delta/\Delta}$ neocortex and hippocampus determined by RNAseq. A, F) Volcano plot displaying gene expression changes detected by DESeq2 in neocortex (A) and hippocampus (F).

Each point represents an individual gene, and all DEGs (FDR<0.05) are highlighted in red (upregulated) or blue (downregulated). The top 10 differentially expressed genes are labelled next to their corresponding position. N=4 mice per genotype, 2 males and 2 females. **B, G)** Heatmap of sequenced genes in neocortical (B) and hippocampal (G) samples. Yellow, upregulated; blue, downregulated. **C, H)** Venn diagrams showing the extent of overlap between DEGs (FDR<0.05), and ASD-associated genes obtained from the SFARI human Gene database. The overlapping genes are shown below the diagram. **D, I)** Venn diagrams showing the extent of overlap between DEGs (FDR<0.05), and ID-associated genes obtained from the Genomics England PanelApp Intellectual disability database. The overlapping genes are shown below the diagram. **E, J)** Gene set enrichment analyses in the neocortex (E) and hippocampus (J) with the top 10 most significant GO terms for both upregulated (activated) and downregulated (supressed) genes.

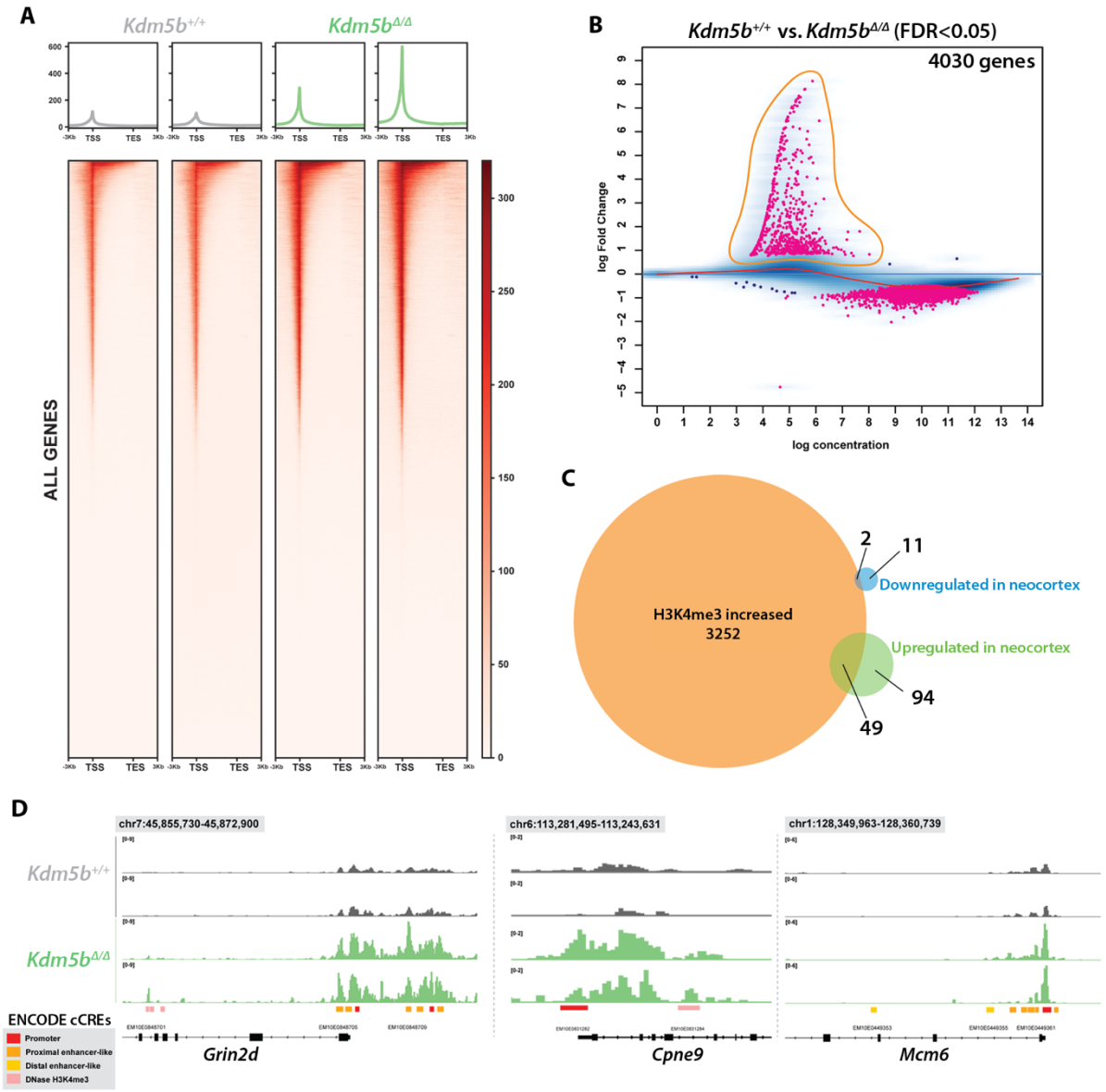

Figure 5. Quantitative CUT&Tag-seq mapping reveals genome-wide increases in H3K4me3 in the neocortex of *Kdm5b*$^{\Delta/\Delta}$ mice. (**A**) Heatmaps of H3K4me3 enrichment around the transcription start site (TSS) of all genes in *Kdm5b*$^{\Delta/\Delta}$ and *Kdm5b*$^{+/+}$ mice (n=2 of each). (**B**) diffBind MA plot identifying gene TSS with significantly (FDR<0.05) altered enrichment between *Kdm5b*$^{\Delta/\Delta}$ and *Kdm5b*$^{+/+}$ mice e. (**C**) Venn diagram overlap of genes identified as differentially expressed between *Kdm5b*$^{\Delta/\Delta}$ and *Kdm5b*$^{+/+}$ mice by bulk RNA-seq and those associated with significantly increased enrichment of H3K4me3 proximal to the TSS. (**D**) IGV genome browser visualisation of H3K4me3 enrichment at the promoters of *Grin2d* and *Mcm6* showing

increases in *Kdm5b*$^{\Delta/\Delta}$ mice. ENCODE candidate cis-regulatory elements (cCREs) are shown to demarcate promoter elements.

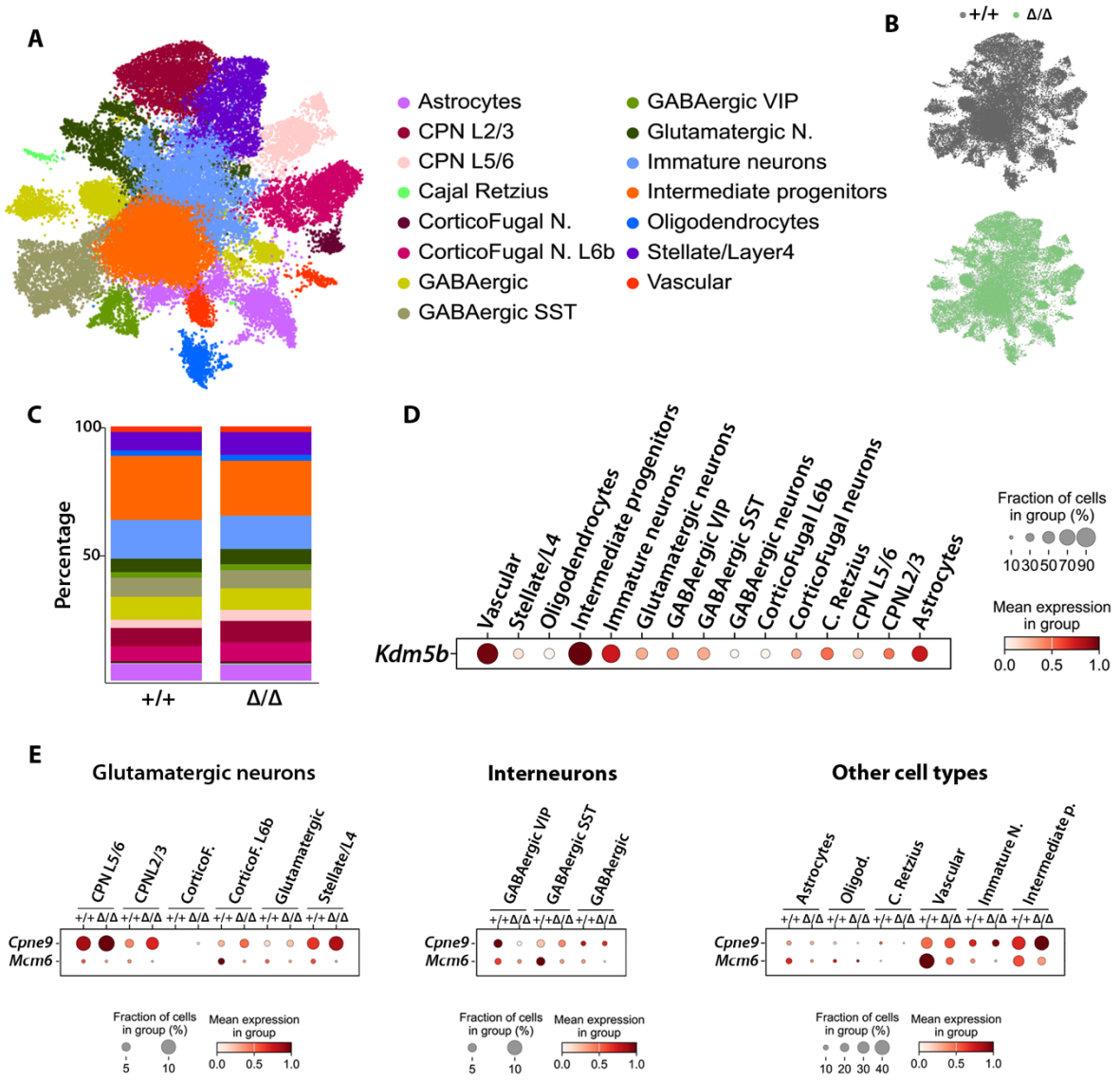

Figure 6. Single nuclei RNA sequencing of control and *Kdm5b* mutant neocortices at PND5. A) UMAP plot revealing the different cell identities in the neocortex. Data derive from 8 +/+ and 8 mutant mice. **B)** Split UMAP revealing the contribution of the cells from each genotype to the broad cellular groups shown in (A). **C)** Analysis of the cellular composition for each genotype does not reveal significant changes in the percentages of any cell population. **D)** Dot plot showing the scaled expression of *Kdm5b* in the different cell populations. **E)** Dot plots showing the scaled expression of *Cpne9* and *Mcm6* (top up- and downregulated genes, respectively, in

the bulk RNAseq experiment) in the different cell populations, grouped as: glutamatergic neurons, interneurons and other cell types.

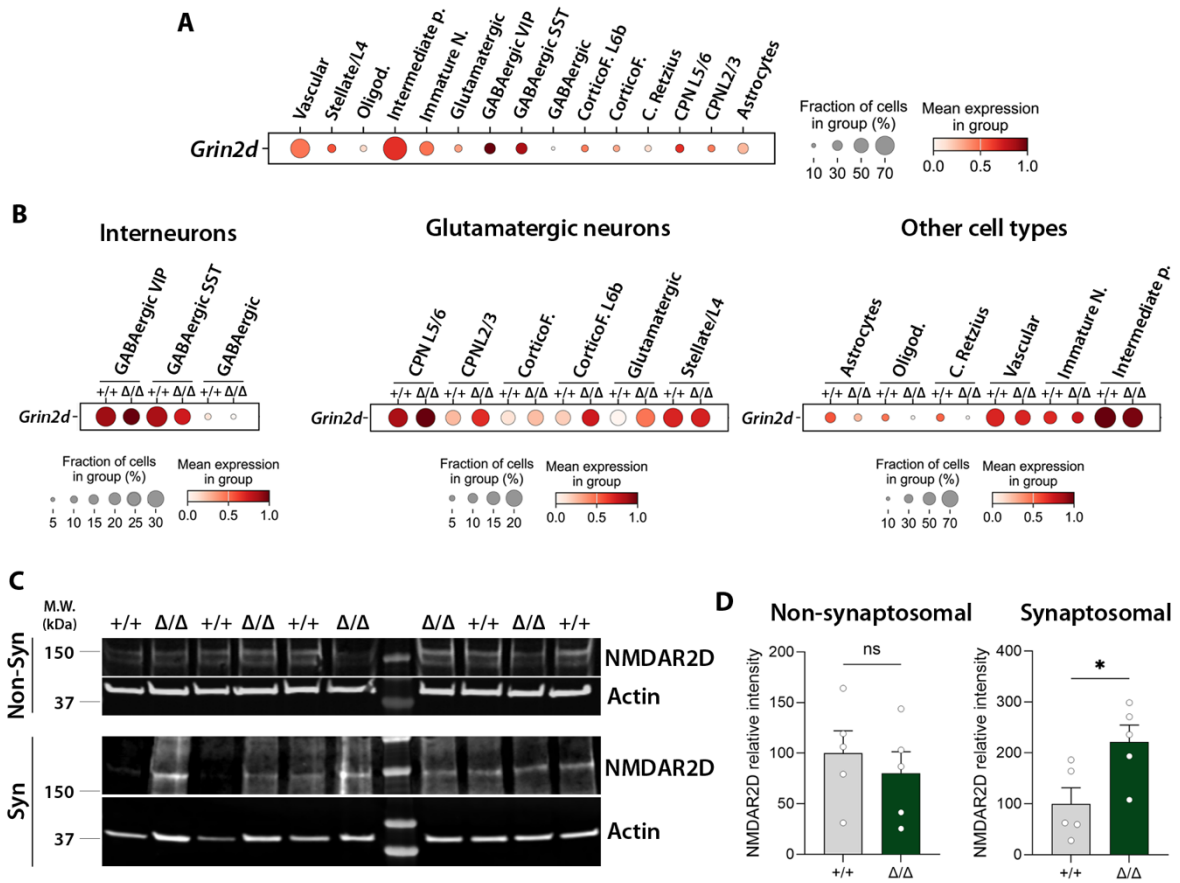

Figure 7. Characterization of the cell types contributing to increased *Grin2d* expression in *Kdm5b* mutant mice. A) Dot plot showing the scaled expression levels of *Grin2d* in the different cell populations in out dataset. **B)** Dot plots showing the scaled expression levels of *Grin2d* in the different cell types (grouped as Interneurons, Glutamatergic neurons and Other cell types) in control (+/+) and mutant (Δ/Δ) mice. **C, D)** Neocortical samples from PND5 mice were dissected and synaptosomes were isolated. Both the non-synaptosomal and the synaptosomal fractions were subjected to western blotting. Membranes were probed for NMDAR2D and β-actin. Molecular weights are shown on the left (C). The densitometric quantification of NMDAR2D levels in both fractions is shown in D. N=5 +/+ and 5 Δ/Δ mice.

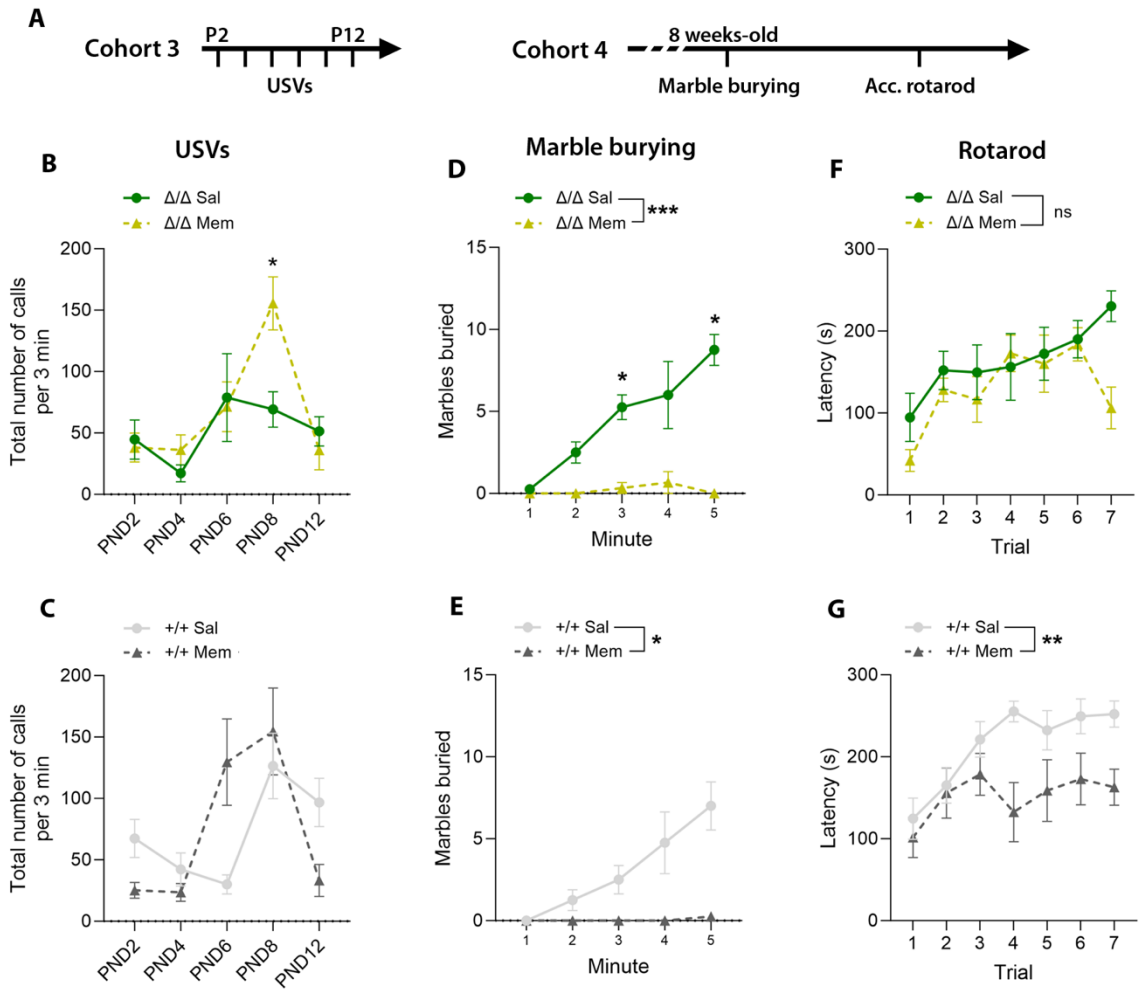

Fig. 8. Memantine ameliorates neonatal communication deficits and digging behaviour in *Kdm5b* mutant mice. A) Experiment design. Two different cohorts were used for neonatal and adult tests. Memantine was administered 30 minutes before the start of the test each day. **B, C)** Total number of ultrasonic vocalizations (USVs) during 3 minutes testing sessions on indicated postnatal days. Repeated measures two-way ANOVA Interaction in B: $F_{(2.603,31.24)}$=3.520, *p=0.0313 followed by Sidak's multiple comparisons test (PND8, *p=0.0313). N= 15 +/+ saline, 13 +/+ memantine, 6 Δ/Δ saline and 8 Δ/Δ memantine. **D, E)** Number of marbles buried during a 5-minute test with 2-months-old mice. Repeated measures Two-way ANOVA treatment effect: $F_{(1,5)}$=99.5, ***p=0.0002 (D) and $F_{(1,6)}$=13.56, *p=0.0103 (E) and interaction effect $F_{(1.314,\ 6.570)}$=5.12, **p=0.0053 (D) and $F_{(4,24)}$=8.387, ***p=0.0002 (E), followed by Sidak's multiple comparisons test. N= 4 +/+ saline, 4 +/+ memantine, 4 Δ/Δ saline and 3 Δ/Δ memantine. **F, G)** Mean latency of mice to fall from the rotarod during 7 trials in one day. Repeated measures Two-way ANOVA treatment effect: $F_{(1,11)}$=1.996, p=0.1854 (F) and $F_{(1,14)}$=10.48, **p=0.006 (G) and interaction effect $F_{(4.166,\ 45.83)}$=1.9,

p=0.1240 (F) and $F_{(3.304,\ 46.26)}$=1.524, p=0.2178 (G). N= 10 +/+ saline, 6 +/+ memantine, 7 Δ/Δ saline and 6 Δ/Δ memantine. Memantine doses were 5.6mg/kg for neonatal animals in the USVs test and 10mg/kg for adult mice. Memantine or saline were administered 30 min before the start of the test. Data is shown as mean ±SEM.